AGU PUBLICATIONS

JGR

Journal of Geophysical Research: Atmospheres

RESEARCH ARTICLE
10.1002/2015JD024135

Key Points:
- Horizontal wavelenghts are derived from radio occultation (RO) data with triples of measurements
- Zonal momentum fluxes from this study are considerably larger than based on profile pairs
- Horizontal detrending with RO and ERA-Interim is more reliable than with vertical detrending

Correspondence to:
T. Schmidt,
torsten.schmidt@gfz-potsdam.de

Citation:
Schmidt, T., P. Alexander, and A. de la Torre (2016), Stratospheric gravity wave momentum flux from radio occultations, *J. Geophys. Res. Atmos.*, *121*, 4443–4467, doi:10.1002/2015JD024135.

Received 26 AUG 2015
Accepted 12 FEB 2016
Accepted article online 17 FEB 2016
Published online 5 MAY 2016

Stratospheric gravity wave momentum flux from radio occultations

T. Schmidt[1], P. Alexander[2], and A. de la Torre[3]

[1]GFZ German Research Centre for Geosciences, Potsdam, Germany, [2]IFIBA, CONICET, Ciudad Universitaria, Buenos Aires, Argentina, [3]Facultad de Ingeniería, Universidad Austral, Buenos Aires, Argentina

Abstract Triples of GPS radio occultation (RO) temperature data are used to derive horizontal and vertical gravity wave (GW) parameters in the stratosphere between 20 km and 40 km from which the vertical flux of horizontal momentum is determined. Compared to previous studies using RO data, better limiting values for the sampling distance ($\Delta d \leq 250$ km) and the time interval ($\Delta t \leq 15$ min) are used. For several latitude bands the mean momentum fluxes (MFs) derived in this study are considerably larger than MF from other satellite missions based on horizontal wavelengths calculated between two adjacent temperature profiles along the satellite track. Error sources for the estimation of MF from RO data and the geometrical setup for the applied method are investigated. Another crucial issue discussed in this paper is the influence of different background separation methods to the final MF. For GW analysis a measured temperature profile is divided into a fluctuation and a background and it is assumed that the fluctuation is caused by GWs only. For the background separation, i.e., the detrending of large-scale processes from the measured temperature profile, several methods exist. In this study we compare different detrending approaches and for the first time an attempt is made to detrend RO data with ERA-Interim data from the European Centre for Medium-Range Weather Forecasts. We demonstrate that the horizontal detrending based on RO data and ERA-Interim gives more consistent results compared with a vertical detrending.

1. Introduction

Gravity waves (GWs) play an important role for the general atmospheric circulation due to the related transport of energy and momentum between different regions of the atmosphere [*Fritts and Alexander*, 2003; *Alexander et al.*, 2010]. The momentum mostly generated in the troposphere is transported to upper atmospheric levels where GWs break or dissipate and transfer their momentum to the background wind (GW drag). The deposit of GW momentum can occur in the complete altitude range from the upper troposphere-stratosphere, the mesosphere [*Fritts et al.*, 2006], and even in the thermosphere [*Heale et al.*, 2014].

A prominent example of GW drag effects in the tropical lower and middle stratosphere is the quasi-biennial oscillation (QBO). The periodic zonal wind reversal can be only explained by consideration of GWs in that region [*Lindzen and Holton*, 1968], whereas their stimulation effect for the QBO can reach up to 70% [*Ern and Preusse*, 2009].

Because of their subgrid scale, GWs generally need to be parametrized in climate models to obtain realistic wind and temperature fields [*Geller et al.*, 2013]. The most important parameter for the description of GW effects on the background winds and atmospheric circulation is the vertical flux of horizontal momentum or GW momentum flux (MF) [*Fritts and Alexander*, 2003]. The MF determination is necessary to estimate the level of wave breaking and hence the effect of GWs on the mean flow [*Geller et al.*, 2013].

A global observation of MF is only possible with satellite data, but a direct measurement from satellites is impossible. It can be indirectly deduced if the MF is written as a function of several parameters obtained by the measurement of temperature profiles [e.g., *Fritts and Alexander*, 2003]. Most of the parameters characterizing GW activity can be derived from single profiles: temperature fluctuations T' or variances T'^2, temperature amplitude $\hat{T}$, vertical wave number k_z or wavelength λ_z, and potential energy E_p, but for MF estimation the horizontal wave number k_h or wavelength λ_h is required. However, both k_h and λ_h cannot be deduced from a single temperature profile alone.

Ern et al. [2004] describe a method for the MF determination along a satellite track by estimation of the phase shift between pairs of neighboring temperature fluctuation profiles: the horizontal wave number k_h at a given altitude is the ratio of the phase shift $\Delta\Phi$ and the distance Δx of the measurements. The method was applied, for example, to satellite data from Cryogenic Infrared Spectrometers and Telescopes for the Atmosphere (CRISTA) [*Offermann et al.*, 1999; *Ern et al.*, 2004], High Resolution Dynamics Limb Sounder (HIRDLS) [*Gille et al.*, 2008; *Alexander et al.*, 2008], and Sounding of the Atmosphere using Broadband Emission Radiometry (SABER) [*Russell et al.*, 1999; *Ern et al.*, 2011]. As described and discussed in detail by *Ern et al.* [2004], the method has two limitations. The first issue is related to the data sampling and the observational window for GWs of the observing satellite system. For each instrument or method for the determination of GWs a lower limit for the detection of horizontal (and also vertical) wavelengths exists [*Wu et al.*, 2006] which is independent of the sampling distance. This means that the real (unknown) GW field may contain horizontal wavelengths shorter than the detection limit or shorter than the Nyquist wavelength ($2\Delta x$) which is the lower limit according to the sampling distance Δx. Insufficient data sampling and temperature fluctuations T' from different waves lead to randomly distributed phase differences $\Delta\Phi$, and horizontal wavelengths in that case are estimated too short near the lower detection limit [*Ern et al.*, 2004]. Second, the derived horizontal wavelengths are "apparent" wavelengths in the direction of both neighboring measurements [*Ern et al.*, 2004; *Alexander et al.*, 2008; *Geller et al.*, 2013]. The "real" horizontal wavelength can differ significantly depending on the angle α between the connecting line of the two profiles and the real horizontal wave vector, whereas the horizontal wavelength along the connecting line is $1/\cos\alpha$ larger than the real horizontal wavelength [*Preusse et al.*, 2002]. For illustration see Figures 2 and 4. This leads to an underestimation of the MF.

Therefore, the profiles used for the GW analysis must be selected with a suitable spatiotemporal sampling including a minimum horizontal sampling limit and at least triples of nearby temperature profiles are necessary to constrain real horizontal wavelengths and momentum fluxes [*Wang and Alexander*, 2010; *Faber et al.*, 2013]. Both issues are subject of this study and will be discussed in detail.

At present, one of the very few satellite data sets able to provide nearby triples of temperature profiles are Global Positioning System (GPS) radio occultations (ROs). The vertical resolution of RO is about 1 km in the stratosphere, whereas the horizontal resolution is about 300 km [*Kursinski et al.*, 1997]. The RO technique as a limb sounding method is sensitive to GWs with small ratios of vertical to horizontal wavelengths [*Wu et al.*, 2006]. Due to the relatively low horizontal resolution and the spherical symmetry assumption in the RO retrieval to derive atmospheric temperature profiles, a weakening of the amplitudes and a vertical phase shift in the temperature profiles occur, whereas the strength of the effect depends on the vertical and horizontal wavelengths and the observation geometry relative to the GW field [*Lange and Jacobi*, 2003; *Alexander et al.*, 2008]. Based on the sensitivity studies by *Lange and Jacobi* [2003], horizontal wavelengths λ_h larger than about 100 km can be detected by the RO technique.

Generally, there is no upper limit for the vertical wavelength of GWs which can undergo considerable Doppler shifting in nonzero background wind, and thereby, they can reach very long vertical wavelengths. Due to the limited height range of the RO data, it is not possible to resolve ultralong vertical wavelengths and the RO retrieval suppresses vertical wavelengths below the vertical resolution of about 1 km in the stratosphere. *Marquardt and Healy* [2005] demonstrated that the lower limit of vertical wavelengths λ_z that can be detected with RO measurements is about 2 km.

Wang and Alexander [2010] applied the method from *Ern et al.* [2004] to clusters of three or more GPS RO temperature profiles from the Formosa Satellite Mission 3/Constellation Observing System for Meteorology, Ionosphere, and Climate (FORMOSAT3/COSMIC; in the following called COSMIC) mission [*Anthes et al.*, 2008; *Anthes*, 2011], but with very large spatial and temporal data sampling limits. Due to the sparse data density of RO data, they allowed more than several hundred kilometer distances between the temperature profiles and also more than 2 h in time between the measurements. *Faber et al.* [2013] introduced an optimized method for the estimation of the horizontal wavelength based on triples of GPS RO temperature profiles but also with broad intervals for the data sampling. The main assumption of the Ern et al. method is that the considered measurements must belong to the same sinusoidal wave or wave pattern. Because of the properties of GWs, a spatiotemporal data sampling over several hundred kilometers is incompatible with the method from Ern et al., in addition, the time interval for sampling the wave should be much shorter than 1 h to avoid phase progression of the wave due to its frequency.

Therefore, in this study we use only triples of GPS RO temperature profiles within a distance of 250 km and a time difference of less than 15 min to better comply the requirement of nearly simultaneous measured profiles.

Alexander [2015] recently published a study for the mean momentum flux distribution between 17 km and 22 km based on temperature triples from combined HIRDLS and COSMIC data. The measurements along the HIRDLS tracks were complemented by nearby (in time and location) COSMIC data. *Alexander* [2015] showed that different temporal (10–20 min) and spatial (200–600 km) sampling lead to a momentum flux variation of only 20%. This is in agreement with our study, but we only use temperature data from GPS RO making the results a different and independent measure of MF as compared when using a combination of different data sets.

Beside the issue of determination of horizontal wave parameters from satellite data, each observation technique to detect GWs needs to separate a background from the measured properties (mostly temperature profiles) in order to remove non-GW contributions from the overall measurements. The non-GW parts are mainly large-scale planetary waves in the extratropics and Kelvin waves in the tropics. Ideally, the remaining temperature fluctuation profiles contain only contributions from GWs. The methods to extract temperature fluctuations from a measured profile are manifold. We also address this topic and compare MF calculations based on vertical [e.g., *Allen and Vincent*, 1995; *Tsuda et al.*, 2000; *Schmidt et al.*, 2008] and horizontal [e.g., *Alexander et al.*, 2008; *Wang and Alexander*, 2010; *Ern et al.*, 2011] detrending methods. This is similar to a comparison performed by *John and Kumar* [2013] for the potential energy, but here we focus on the momentum flux. In addition to that, we use for the first time ERA-Interim data [*Dee et al.*, 2011] as a background temperature climatology for detrending GPS RO data.

In section 2 we describe the RO data set and in section 3 the observation geometry. The method to derive MF and the different detrending methods are presented in sections 4 and 5. In section 6 we outline the data processing for the GW analysis performed in this study, and in section 7 a detailed discussion of several GW parameters is given. A comparison between GW parameters derived with different data sampling limits and different detrending methods is performed in section 8.

2. Database

A detailed description of methods used to derive vertical atmospheric profiles from RO measurements is presented by *Kursinski et al.* [1997]. Here a brief summary is given. The GPS receiver on board a Low-Earth Orbiting (LEO) satellite records phase and amplitude variations with high temporal resolution (e.g., 50 Hz) during an occultation event. By using high-precision orbit information from the LEO and the occulting GPS satellite, the atmospheric excess phase can be extracted which is related to a bending angle profile. Assuming spherical symmetry, the bending angles can be related to the refractive index n, and finally, the atmospheric refractivity N_{ref} is given by [*Smith and Weintraub*, 1953]

$$N_{\mathrm{ref}} = (n-1)\cdot 10^6 = 77.6\frac{p}{T} + 3.73\cdot 10^5 \frac{e_w}{T^2} \tag{1}$$

(p: total air pressure, T: air temperature, and e_w: water vapor pressure).

To convert the refractivity profiles into pressure and temperature profiles, the assumption of dry air has to be made because of the ambiguity between the dry and wet parts in the resulting refractivity (equation (1)). Further on, by applying the hydrostatic equation, pressure and temperature profiles can be calculated. The dry air assumption is justified here because we perform our analysis in the stratosphere between 20 km and 40 km where humidity effects are negligible.

In this study we use the reprocessed RO data from UCAR (University Corporation for Atmospheric Research) for the time interval from May to October 2006. The data are freely available on http://cdaac-www.cosmic.ucar.edu/cdaac/products.html.

As discussed in section 1, the application of the method from *Ern et al.* [2004] for the derivation of horizontal wavelengths between two measurements requires a suitable spatiotemporal sampling because in both temperature fluctuation profiles the same GW pattern must be present. In addition, to constrain real

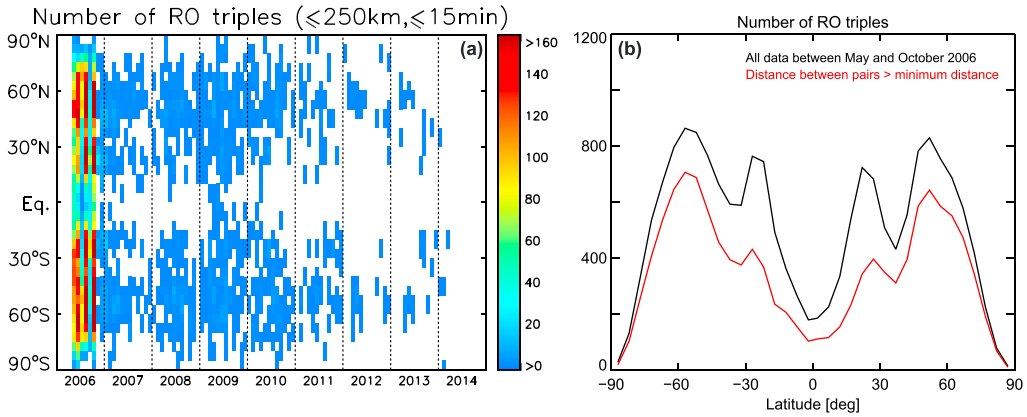

Figure 1. (a) Zonal monthly number of profile triples with a distance $\Delta d \leq 250$ km and a time difference $\Delta t \leq 15$ min based on CHAMP, COSMIC, and Metop-A radio occultations. (b) Zonal number of profile triples ($\Delta d \leq 250$ km and $\Delta t \leq 15$ min) between May and October 2006 for all triples (black) and triples formed by pairs with the minimum sampling distance after equation (4) (red). The interval width is 5°.

horizontal wavelengths, triples of temperature profiles are necessary. Based on the results from *Wang and Alexander* [2010], *Faber et al.* [2013], and more recently from *Alexander* [2015], we use in our study a maximum distance of 250 km and a maximum time difference of 15 min between the measurements.

The reprocessed RO data set from UCAR contains data from the six COSMIC satellites (2006–2014), the Challenging Minisatellite Payload (CHAMP, 2001–2008), and the Meteorological Operational Polar Satellite-A (Metop-A, 2007–2011).

Based on this data set, Figure 1a shows the zonal monthly number of temperature profile triples between May 2006 and April 2014 with a distance Δd less than 250 km and a time interval Δt less than 15 min between the individual profile pairs forming the triple. Before 2006 only CHAMP data with insufficient data density are available. Between the COSMIC launch in April 2006 and October 2006 where all COSMIC satellites were close together, the number of triples is enhanced, but after reaching the final orbit positions of the six satellites, the number of triples decreases significant. For this reason we limit our data analysis to the early mission time of COSMIC because only during that time period the data density of nearby ($\Delta d \leq 250$ km and $\Delta t \leq 15$ min) temperature triples is sufficient for a significant statistic of horizontal wavelengths and momentum fluxes. The solid black line in Figure 1b shows the zonal number of all RO triples between May and October 2006, and we limit our results to zonal mean values.

3. Observation Geometry

Compared to previous studies using RO data for the determination of horizontal wavelengths and momentum fluxes [*Wang and Alexander*, 2010; *Faber et al.*, 2013], we use stronger limits for the maximum sampling distances and sampling time intervals that are better in agreement with the requirements of the method from *Ern et al.* [2004].

In contrast to regularly spaced measurements from CRISTA, HIRDLS, or SABER, the RO data are nonuniformly distributed and the line of sight (LOS) between the GPS and LEO satellites can vary within a triple of temperature profiles. If combining soundings with different LOS directions and allowing sampling with nonzero time difference (15 min here), then also a minimum horizontal sampling limit or a minimum phase shift difference must be introduced to avoid horizontal wavelengths being dominated by random effects [*Preusse et al.*, 2002]. *Faber et al.* [2013] introduced a minimum value of 0.5 rad (about 29°) for vertical phase differences between two temperature fluctuation profiles. Below we define a latitude-dependent minimum horizontal sampling limit, which will be justified in the next two sections.

3.1. LOS Conditions

Different LOS conditions influence the deduced temperature amplitudes and horizontal wavelengths and finally the MF [*Preusse et al.*, 2002; *Lange and Jacobi*, 2003]. Figure 2a illustrates three cases of LOS directions relative to the horizontal wave vector. When the GPS signal propagates parallel to the horizontal wave vector

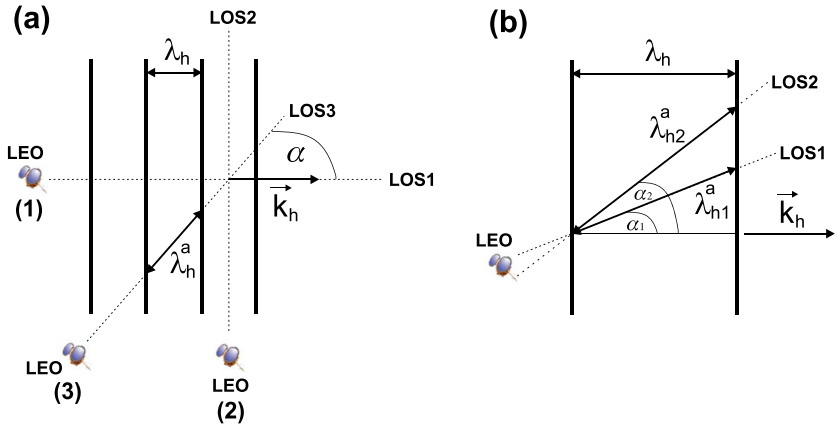

Figure 2. (a) Schematic of the horizontal projection of a gravity wave with horizontal wavelength λ_h and three cases of line-of-sight (LOS) conditions relative to the horizontal wave vector $\vec{k_h}$. (1) LOS in the direction of $\vec{k_h}$, the angle $\alpha(\vec{k_h}, \mathrm{LOS}) = 0°$ (LOS perpendicular to the wave crests), (2) LOS perpendicular to $\vec{k_h}$, $\alpha(\vec{k_h}, \mathrm{LOS}) = 90°$ (LOS parallel to the wave crests), and (3) LOS and $\vec{k_h}$ forming an angle α between 0° and 90°. (b) Similar to Figure 2a but for two LOS examples forming two angles α_1 and α_2 between 0° and 90°. The λ_h^a are the apparent horizontal wavelengths in the direction of the LOS.

$\vec{k_h}$ (case 1), the resulting apparent horizontal wavelength λ_h^a is in agreement with the true horizontal wavelength λ_h. On the other hand, in this constellation the weakening of the temperature amplitude is largest because the positive and negative phase variations are canceled out along the signal path [*Lange and Jacobi*, 2003; *Alexander et al.*, 2008]. The other extreme is if the LOS is perpendicular to the horizontal wave vector $\vec{k_h}$ (case 2), the observed amplitude converges to its maximum value, but the horizontal wavelength approaches to infinity. In most of the cases the LOS will be probably between 0° and 90° in relation to the true (unknown) horizontal wave vector (case 3).

Considering this effect, temperature fluctuations and temperature amplitudes derived from RO data are mostly underestimated with consequences for potential energy and momentum flux distributions.

Another issue arises if soundings with different viewing directions are combined. In this case the bias of the vertical phase will be different for the different soundings [*Preusse et al.*, 2002; *Lange and Jacobi*, 2003]. This introduces quasi-random phase errors that have to be considered if the phase shift between two profiles is used. For the estimation of this error for the RO data set Figure 3a shows the histogram of all LOS differences between each profile pair used in this study. The differences are restricted between 0° and 90°, because the LOS has no forward or backward direction. The median of the distribution is less than 1°, and the mean LOS difference between individual pairs is about 4°. Eighty-seven percent of all pairs exhibit a LOS difference less than the mean value. Zonal mean LOS differences between profile pairs are small in the tropics and reach values of about 5°–6° in the high latitudes of both hemispheres (Figure 3b). The close LOS values are caused by the fact that during the beginning of the COSMIC mission the six satellites were close together and the single-occultation measurements forming a triple were performed with mostly the same GPS satellite.

Figure 2b illustrates the influence of different LOS directions on the apparent horizontal wavelength. If there is an angle α_1 between the first LOS (LOS1) and the (true) horizontal wave vector and a second angle α_2 between the LOS and the wave vector (LOS2), then the ratio of the two apparent horizontal wavelengths parallel to each LOS $\lambda_{h2}^a / \lambda_{h1}^a = \cos\alpha_1 / \cos\alpha_2$. From the LOS analysis (Figures 3a and 3b) we found that the mean LOS difference between two profiles is about 4°. Now let us consider some cases of what could happen within a 90° interval of orientations between LOS and observed wave:

(a) $\alpha_1 = 0°, \alpha_2 = 4° \rightarrow \lambda_{h2}^a / \lambda_{h1}^a = \cos\alpha_1 / \cos\alpha_2 = 1.00$
(b) $\alpha_1 = 4°, \alpha_2 = 8° \rightarrow \lambda_{h2}^a / \lambda_{h1}^a = \cos\alpha_1 / \cos\alpha_2 = 1.01$
(c) $\alpha_1 = 8°, \alpha_2 = 12° \rightarrow \lambda_{h2}^a / \lambda_{h1}^a = \cos\alpha_1 / \cos\alpha_2 = 1.01$
(d) $\alpha_1 = 12°, \alpha_2 = 16° \rightarrow \lambda_{h2}^a / \lambda_{h1}^a = \cos\alpha_1 / \cos\alpha_2 = 1.02$
…
(e) $\alpha_1 = 76°, \alpha_2 = 80° \rightarrow \lambda_{h2}^a / \lambda_{h1}^a = \cos\alpha_1 / \cos\alpha_2 = 1.39$
(f) $\alpha_1 = 80°, \alpha_2 = 84° \rightarrow \lambda_{h2}^a / \lambda_{h1}^a = \cos\alpha_1 / \cos\alpha_2 = 1.66$

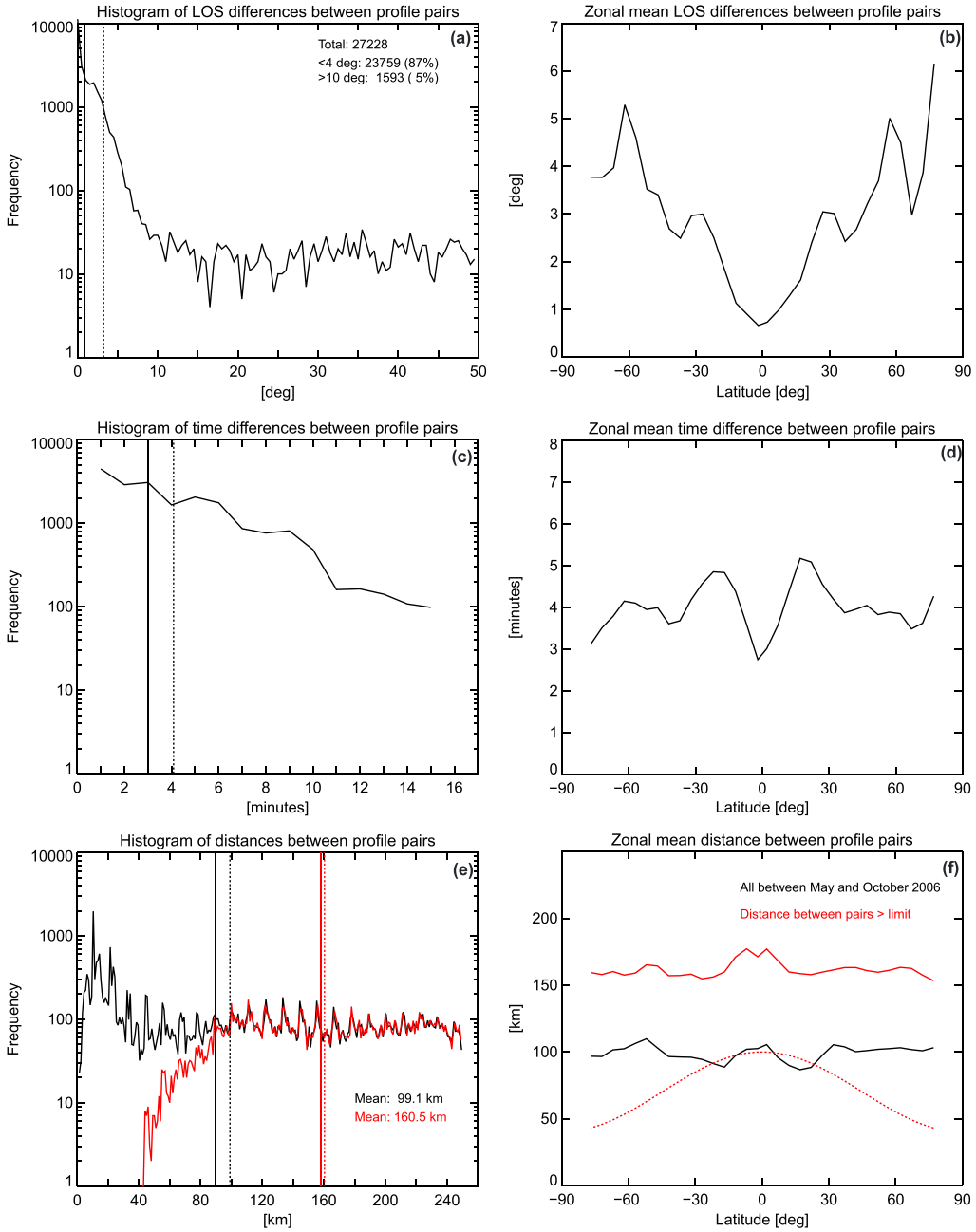

Figure 3. (a) Histogram of LOS difference between individual profile pairs within the triples of profiles with $\Delta d \leq 250$ km and $\Delta t \leq 15$ min between May and October 2006. (b) Zonal mean LOS differences between pairs. (c) Histogram of time difference between profile pairs. (d) Zonal mean time difference between profile pairs. (e) Histogram of distances between profile pairs for all (black) pairs ($\Delta d \leq 250$ km and $\Delta t \leq 15$ min) and with the minimum sampling distance according to equation (4) (red). (f) Zonal mean sampling distances between all (black) profile pairs and for pairs with the application of the minimum sampling distance (solid red). The dotted red line denotes the minimum sampling distance according to equation (4). In Figures 3a, 3c, and 3e the vertical solid line and the vertical dotted line denote the median and mean of the distribution, respectively.

(g) $\alpha_1 = 84°, \alpha_2 = 88° \rightarrow \lambda^a_{h2}/\lambda^a_{h1} = \cos\alpha_1/\cos\alpha_2 = 2.99$
(h) $\alpha_1 = 88°, \alpha_2 = 90° \rightarrow \lambda^a_{h2}/\lambda^a_{h1} = \cos\alpha_1/\cos\alpha_2$

In the most favorable constellations (a)–(d) the true and apparent wavelengths are almost the same. In the less favorable constellations (e)–(h), however, the wavelength can be different, mainly if both LOS directions and the observed wavefield form angles larger than 80°. A mean value $\lambda^a_{h2}/\lambda^a_{h1}$ for all combinations between

the angles listed above is 1.3. This value is only exceeded by combinations α_1 and α_2 larger than 76°. According to *Lange and Jacobi* [2003] (their Figure 2b) and for a typical vertical wavelength from RO data of 8 km for λ^a_{h1}=500 km (λ^a_{h2} would be then 650 km), a phase shift of about 12° occurs. Anticipate our results for the horizontal wavelengths (Figures 6d and 8c) [*Preusse et al.*, 2006], λ_h= 500 km is a lower value within the standard deviation for high latitudes. For larger horizontal wavelengths the phase shift is reduced [*Lange and Jacobi*, 2003]; e.g., for the combination λ^a_{h1}= 800 km and λ^a_{h2} = 1040 km a phase shift of about 5° occurs. One should also note that *Lange and Jacobi* [2003] performed their simulations for the unfavorable case (1) in Figure 2a; i.e., the LOS is in line with the horizontal wave vector and the amplitude damping is largest. This means that a phase shift error of 12° due to the combination of measurements with different LOS directions is considered a maximum value.

3.2. Temporal Data Sampling

Another source of error for the phase shift calculations between two adjacent temperature fluctuation profiles is introduced due to the allowed sampling time limit of 15 min. For an estimation of this phase error we consider the dispersion relation for the middle atmosphere [*Fritts and Alexander*, 2003]:

$$\hat{\omega}^2 = \frac{N^2 \cdot k_h^2}{m^2} \tag{2}$$

with $\hat{\omega}$ as the intrinsic frequency, N the Brunt-Väisälä frequency, and k_h and m as the horizontal and vertical wave numbers. Equation (2) can be rewritten as

$$\frac{T_N}{T_{\mathrm{GW}}} = \frac{\lambda_z}{\lambda_h} \tag{3}$$

with $T_N = 2\pi/N$ and $T_{\mathrm{GW}} = 2\pi/\hat{\omega}$ as the Brunt-Väisälä period and the intrinsic period of the GW, respectively.

Supposing a mean $N = 0.02s^{-1}$ in the stratosphere [*Schmidt et al.*, 2010] and a typical vertical wavelength λ_z of 8 km, the GW intrinsic period for a horizontal wavelength λ_h=500 km (high latitudes) is about $T_{500\mathrm{km}}$=5.4 h and for λ_h=1600 km (tropics) $T_{1600\mathrm{km}}$=17.4 h.

The maximum sampling time difference is 15 min. From Figures 3c and 3d follows that the mean time difference between all pairs is about 4 min (median = 3 min), i.e., 0.07 h. During this time period the phase of the wave will progress by (0.07 h/5.4 h) · 360° = 4.7° at high latitudes and (0.07 h/17.4 h) · 360° = 1.4° in the tropics. The multiplication with 360° is due to the relation to a full wave period or wavelength.

Thus, the phase error introduced by the sampling within 15 min is supposed to be about 5°.

3.3. Minimum Horizontal Sampling Limit

Phase errors introduced by the combination of measurements with different LOS (about 12° error) and with an allowed maximum time difference of 15 min (about 5° error) lead to a total error of about 17°.

Seventeen degrees correspond to about 1/21 full wave period or full wavelength, and the shortest horizontal sampling distance that would be allowed has to exceed at least 1/21 the horizontal wavelength λ_h. Assuming a mean high-latitude λ_h of 800 km (Figure 6d) [*Preusse et al.*, 2006], the sampling distance has to exceed at least about 40 km. For low latitudes (λ_h about 2000 km) the minimum sampling distance increases to about 100 km.

Figure 3e shows the histogram of distances between profiles for the complete data set between May and October 2006 (solid black line). The mean distance is about 99 km, and there is nearly no latitudinal variation (Figure 3f).

With the results for the error discussion related to the phase of the measurements we construct a simple latitude (ϕ)-dependent minimum horizontal sampling distance in kilometers:

$$\Delta x_{\mathrm{min}} = 70 + 30 \cdot \cos(2\phi) \tag{4}$$

Thus, Δx_{min} varies between 40 km at the poles and increases to 100 km at the equator (dotted red line in Figure 3f). If only profile pairs exceeding the limit given by equation (4) are used (solid red line in Figures 3e and 3f), the mean distance between the pairs increases to about 160 km. The solid red line in Figure 1b shows the zonal number of triples after applying the minimum horizontal sampling distance to the individual pairs of profiles within the triple. This number of RO triples is the basis for the determination of zonal mean momentum fluxes following the method from *Ern et al.* [2004].

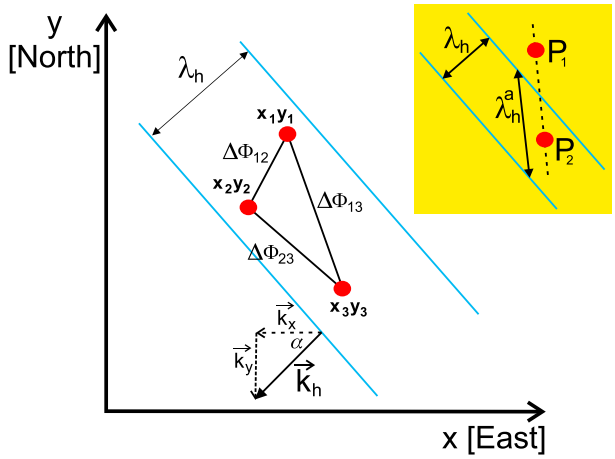

Figure 4. Schematic of the arrangement of radio occultation triples for the determination of the absolute horizontal wave number K_h and the orientation α. The blue lines represent the wave phases, whereas Φ_{ij} is the phase shift between two temperature fluctuation profiles at the constant altitude z. x_iy_i denotes the position and λ_h the horizontal wavelength.

4. Method for the Horizontal Wavelength Estimation

As a summary of the error discussion related to the combination of RO measurements with different LOS and sampling times and the application of the method from *Ern et al.* [2004], the following sampling conditions for each profile pair forming a triple of measurements are

1. The time difference between each profile pair is less than 15 min.
2. The distance between the profiles pairs is less than 250 km.
3. The minimum sampling distance is latitude dependent after equation (4), i.e., 40 km at the poles and 100 km at the equator.

The observing geometry for a triple of measurements is shown in Figure 4 for a constant altitude z. The positions of the three ROs (red points) are denoted with x_1y_1, x_2y_2, and x_3y_3, and the blue lines represent lines of constant phase (wavefronts) of the presumed GW.

On the right-hand side of Figure 4 (yellow background) the difference between the real (λ_h) and the apparent (λ_h^a) horizontal wavelength along points P_1 and P_2 is shown similar to Figure 2a. One can clearly see that in this case the estimated horizontal wavelength along the profile pair is larger than the real horizontal wavelength λ_h of the GW field.

Following the method from *Ern et al.* [2004], the horizontal wave number k_h and the horizontal wavelength λ_h can be expressed by

$$k_h = \frac{\Delta\Phi_{ij}}{\Delta x_{ij}} \quad \text{and} \quad \lambda_h = \frac{2\pi}{|\vec{k}_h|} \tag{5}$$

with $\Delta\Phi_{ij}$ and Δx_{ij} as the phase shift between the temperature fluctuation profiles and the distance of the profiles, respectively, at the same altitude. If Δx_{ij} falls below the minimum sampling limit Δx_{min} according to equation (4), the profile pair and triple are rejected.

Supposing a monochromatic wave, the temperature fluctuation profile can be written as [*Ern et al.*, 2004]

$$T'(x, y, z, t) = \hat{T}(z) \cdot \sin(kx + ly + mz - \omega t) \tag{6}$$

with $\hat{T}$ as the temperature amplitude and the phase Φ:

$$\Phi = kx + ly + mz - \omega t \tag{7}$$

In equations (6) and (7) k and l denote the x and y components of the horizontal wave number k_h (Figure 4), m the vertical wave number, and ω the wave frequency.

The phase difference between two temperature fluctuation profiles at a constant altitude with the same m is then given by

$$\Delta\Phi_{ij}(z) = k \cdot (x_i - x_j) + l \cdot (y_i - y_j) - \omega \cdot (t_i - t_j) \tag{8}$$

Neglecting the time in equation (8), i.e., consider nearly simultaneous observations, the phase difference between two profiles i and j simplifies to

$$\Delta\Phi_{ij}(z) = k \cdot (x_i - x_j) + l \cdot (y_i - y_j) \tag{9}$$

As described in detail in *Faber et al.* [2013] each point of the measurement triple serves as a reference point; i.e., equation (9) is solved three times. For example, if x_1y_1 (Figure 4) is the reference point, the following linear equation system is given and solved for k and l:

$$\begin{aligned}\Delta\Phi_{12}(z) &= k \cdot (x_1 - x_2) + l \cdot (y_1 - y_2)\\ \Delta\Phi_{13}(z) &= k \cdot (x_1 - x_3) + l \cdot (y_1 - y_3)\end{aligned} \tag{10}$$

Thus, for each reference point a horizontal wave number $k_{h1,h2,h3}=(k^2 + l^2)^{0.5}$ can be estimated. If the inner angles of the triangle defined by the three measurements are acute (one of them is obtuse), the three determined $k_{h1,h2,h3}$ values coincide (one of them must be shifted to agree with the remaining two). For more details, we refer to Figures 3 and 4 in *Faber et al.* [2013]. Summarized from the single $k_{h1,h2,h3}$ values and the observation geometry, the absolute horizontal wave number $k_h=(k^2 + l^2)^{0.5}$ and the wave orientation $\alpha=\tan^{-1}(l/k)$ can be calculated (Figure 4) and finally the momentum flux (MF) [*Ern et al.*, 2004]:

$$\mathrm{MF} = \frac{\rho}{2} \cdot \frac{\lambda_z}{\lambda_h} \cdot \left(\frac{g}{N}\right)^2 \cdot \left(\frac{\hat{T}}{\bar{T}}\right)^2 \tag{11}$$

ρ is the background density, λ_z is the vertical wavelength, g is the acceleration due to gravity, and $\hat{T}$ and $\bar{T}$ are the temperature amplitude and background temperature. For the detailed derivation and discussion of the MF equation follow Appendix A of *Ern et al.* [2004].

It should be noted here that the wave orientation α has an ambiguity of 180° and therefore only absolute momentum fluxes can be calculated instead of net momentum fluxes.

Although the momentum flux (MF) estimation has the focus in this study, we also discuss briefly the potential energy E_p as a parameter for the characterization of GW activity but refer for a detailed discussion to the extensive literature [e.g., *Tsuda et al.*, 2004; *de la Torre et al.*, 2006; *Baumgaertner and McDonald*, 2007; *Froehlich et al.*, 2007; *Hei et al.*, 2008]. After *Ern et al.* [2004] the potential energy from a single RO temperature profile can be estimated by

$$E_p = \frac{1}{2} \cdot \left(\frac{g}{N}\right)^2 \cdot \left(\frac{\hat{T}}{\bar{T}}\right)^2 \tag{12}$$

If one combines equations (11) and (12), the momentum flux can be expressed by

$$\mathrm{MF} = \rho \cdot \frac{\lambda_z}{\lambda_h} \cdot E_p \tag{13}$$

5. Detrending

Beside the general discussion of GW detection due to the observation geometry, an additional issue arises with the necessary background separation, i.e., the detrending of large-scale processes from the measured temperature profile. According to the linear theory of GWs [see, e.g., *Nappo*, 2002; *Fritts and Alexander*, 2003], the measured temperature profile $T(z)$ is expanded into a background temperature $\bar{T}(z)$ and a perturbation $T'(z)$ which can be considered as a fluctuation or perturbation:

$$T'(z) = T(z) - \bar{T}(z) \tag{14}$$

The background is assumed to be steady, the fluctuations are much smaller than the background, and the fluctuations should not affect the background. Usually, T' is assumed to be due entirely to GWs, but the correctness of this assumption depends strongly on the background separation approach.

John and Kumar [2013] found significant differences in the GW potential energy magnitudes estimated by horizontal and vertical detrending methods. By comparing COSMIC and SABER stratospheric E_p values, the authors found that most of the differences can be attributed to the detrending method and fewer to the (different) derived SABER and COSMIC temperatures. We perform a similar analysis for different GW parameters, but with the focus to the momentum flux.

In this study we assess three different methods for the determination of $\bar{T}$: (1) horizontal detrending with radio occultations itself [*Wang and Alexander*, 2010], (2) horizontal detrending with ERA-Interim temperatures (same method as (1) but with the ERA-Interim temperature climatology), and (3) vertical detrending using a band-pass filter between 2 km and 15 km [*Tsuda et al.*, 2000].

The first and last methods are well established, but the utilization of ERA-Interim data for the detrending is novel.

For the horizontal detrending the RO and ERA-Interim temperatures were separated into 10° by 5° longitude-latitude bins over a period of 3 days (RO) and 1 day (ERA-Interim). The larger temporal sampling interval for the ROs is necessary because the data density on some days is not sufficient leading to gaps in daily climatologies. For the ERA-Interim data the complete set of daily 6-hourly analyses with 1° by 1° longitude-latitude resolution was used.

Vertically, the data were binned to a regular grid of 100 m between 20 km and 40 km, i.e., in the lower and middle stratosphere. We definitely exclude the tropopause region here to avoid biases in the temperature fluctuation profile when applying a vertical filter to the sharp vertical structure of the thermal tropopause [*Schmidt et al.*, 2008].

For the RO and ERA-Interim temperature climatologies the *S* transform is performed for each latitude as a function of longitude, constructing zonal wave numbers 0–6 as a function of longitude. These zonal wave numbers are used as the large-scale temperature variations (background) $\bar{T}$ that are subtracted from the measured profile T (equation (14)). The resulting temperature fluctuations T' include horizontal fluctuations shorter than wave number 6 [*Wang and Alexander*, 2010; *Faber et al.*, 2013].

6. Data Processing

Figure 5 shows as an example of the single steps (after detrending) from temperature fluctuations (Figure 5a) to momentum flux and wave orientation (Figures 5e and 5f). The detrending for the results discussed below is based on the horizontal detrending approach with RO data. In section 8.3 we present differences in GW parameters estimated from different detrending methods. The temperature amplitude $\hat{T}$, vertical wavelength λ_z, and phase Φ are obtained from a wavelet analysis for each single profile between 20 km and 40 km, whereas the dominant wave in each profile is determined at the power spectrum maximum at each altitude. The results are vertical profiles of $\hat{T}$, λ_z (Figure 5b), and Φ, from which the phase differences between each pair are estimated (Figure 5c). The vertical wavelength between profile pairs must be within 2 km for each altitude, otherwise the wave structures in the single profiles are considered to be caused by different GWs. This follows the approach from *Ern et al.* [2011] and is comparable with the data analysis for the SABER and HIRDLS2 data set in the momentum flux comparison study from *Geller et al.* [2013]. We will refer to this study later again.

For the further processing at each altitude level the mean vertical wavelength based on the three single λ_z values for each altitude is estimated, and for the temperature amplitude the maximum value from the three single $\hat{T}$ values at the same altitude is taken (Figure 5b). The latter is due to the already discussed general underestimation of the temperature amplitude from RO data.

Beside the close spatiotemporal sampling of the temperature triples (as the main requirement for the Ern et al. method) and the application of the minimum sampling criterion (equation (4)), additional quality and plausibility checks are performed during the processing:

1. The maximum difference between the vertical wavelength of each single profile between 20 km and 40 km must be less than 2 km (Figure 5b). This should ensure that the same wave pattern is included in the profile pair [*Ern et al.*, 2004, 2011] and in the triple.

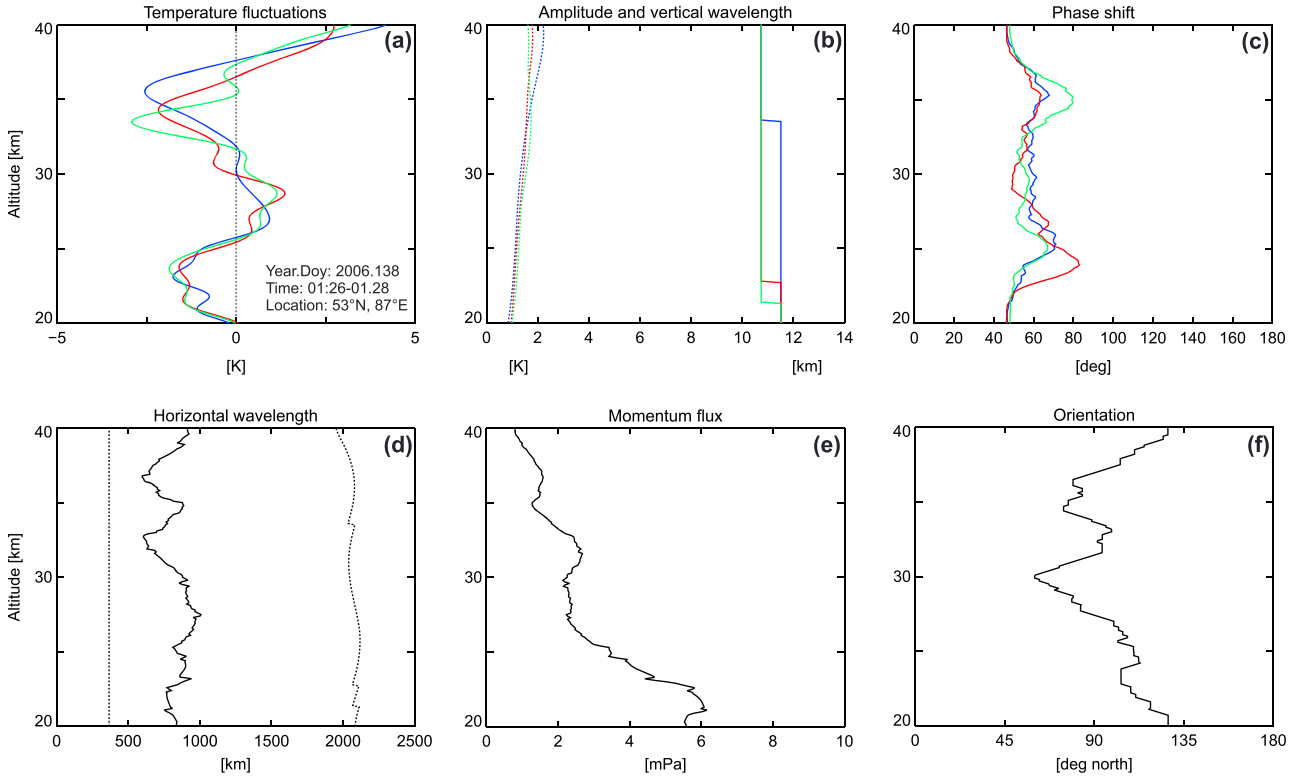

Figure 5. Example for data analysis. (a) Three temperature fluctuation profiles satisfying the spatiotemporal and LOS conditions. (b) Derived temperature amplitude (left) and vertical wavelength (right) from a wavelet analysis for each temperature fluctuation profile. (c) Phase shift between two temperature fluctuation profiles for the three combinations (1–2, 1–3, and 2–3) of temperature fluctuation pairs. (d) The resulting horizontal wavelength (solid line) after equation (5). The right dotted line shows the maximum horizontal wavelength according to equation (15) and the left dotted line the minimum horizontal wavelength (twice the Nyquist wavelength) according to the distances between the profiles. (e) The absolute momentum flux after equation (11). (f) The orientation of the wave. For details see text.

2. The estimated absolute phase shift between each of the three combinations of measurements (Figure 5c) must be in the range 0 and π [*Ern et al.*, 2004].
3. The final estimated horizontal wavelength (Figure 5d) must be larger than twice the Nyquist wavelength $\lambda_{h,\min} = 2 \cdot \Delta x_{ij}$ with Δx_{ij} as the largest distance between two profiles within the triple (left dotted line in Figure 5d) [*Ern et al.*, 2004; *Preusse et al.*, 2006] or larger than the lower limit of horizontal wavelengths (100 km) that can be detected by the radio occultation technique [*Lange and Jacobi*, 2003; *Wu et al.*, 2006].

The right dotted line in Figure 5d represents the maximum horizontal wavelength limited by the Coriolis parameter f. For illustration one can consider the dispersion relation for the middle atmosphere (equation (2)) and because of the limitation of the intrinsic frequency by the Brunt-Väisälä frequency N and the Coriolis parameter f ($N > |\hat{\omega}| > |f|$) for $|\hat{\omega}| = |f|$ (i.e., $|\hat{\omega}|/|f| = 1$) the horizontal wavelength λ_h exhibits an upper boundary $\lambda_{h,\max}$ [*Preusse et al.*, 2006]:

$$\lambda_{h,\max} = \frac{N \cdot \lambda_z}{f} \tag{15}$$

$\lambda_{h,\max}$ in Figure 5d is based on measured N and λ_z values. We return to this issue later during the discussion of the zonal mean horizontal wavelength (Figure 6d).

7. Results and Discussion

Based on the horizontal detrending with radio occultation data described in section 5, zonal mean GW parameters are derived and discussed. The discussion involves the main parameters for the determination of the momentum flux (equation (11)), and the focus is on the horizontal wavelength and the momentum flux, but other GW parameters will be also presented. The results are based on temperature triples with the application of the latitudinal minimum sampling distance after equation (4). The zonal distribution of the number of

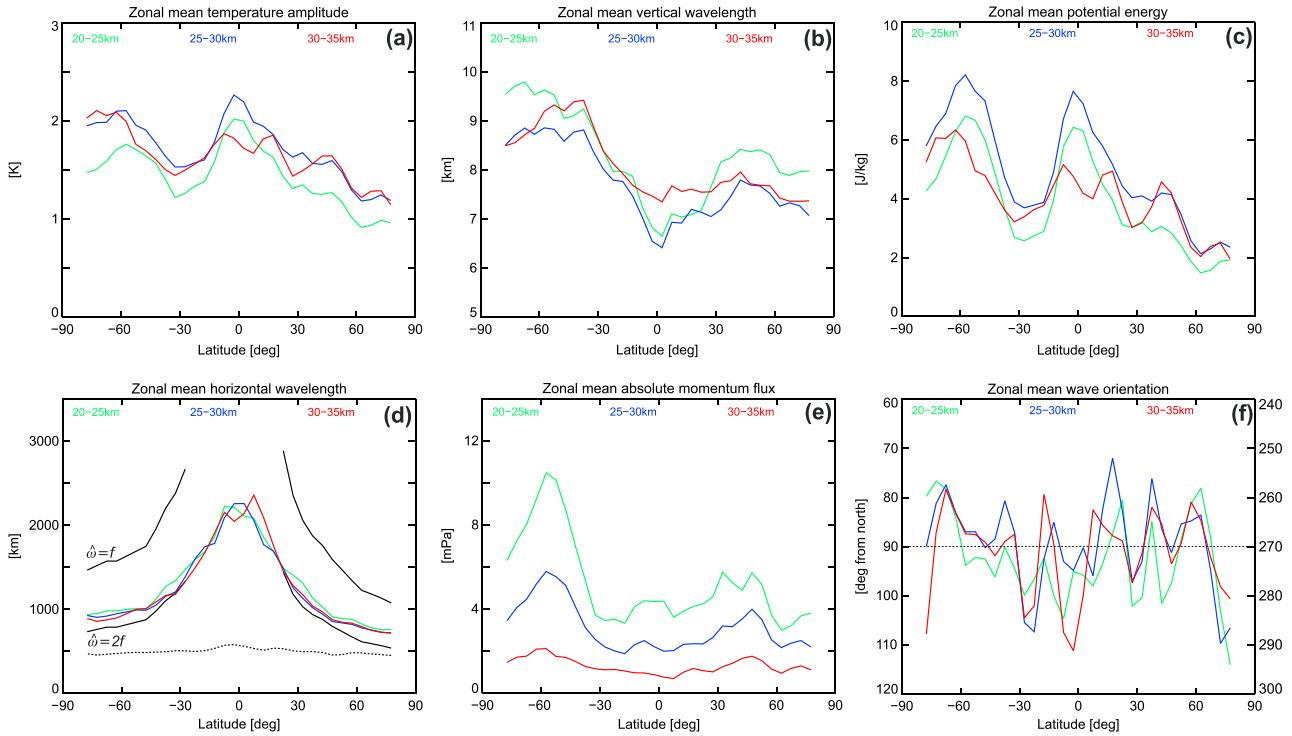

Figure 6. (a) Zonal mean temperature amplitude $\hat{T}$ for different altitude intervals based on the time period May to October 2006 and horizontal detrending with RO data. (b) For the vertical wavelength λ_z. (c) For the potential energy E_p. (d) For the horizontal wavelength λ_h. The black solid lines are theoretical horizontal wavelengths with $\hat{\omega}/f=1$ and $\hat{\omega}/f=2$. The dotted line represents twice the Nyquist wavelength. (e) For the absolute momentum flux (MF). (f) For the zonal mean wave orientation. The direction of the wave can only be determined with a 180° ambiguity; i.e., both the left or right units could be applied. For details see text.

triples is given by the solid red line in Figure 1b. All GW parameters are averaged over three different altitude intervals in the lower and middle stratosphere (20–25 km, 25–30 km, and 30–35 km) to allow the discussion of properties of GW parameters in different parts of the stratosphere.

7.1. Temperature Amplitude $\hat{T}$

The GW momentum flux is proportional to the squared temperature amplitude (equation (11)), and therefore, the amplitude is a key parameter that determines mainly the momentum that a GW carries from the source region to upper atmospheric levels. This makes the amplitude, beside the vertical and horizontal wavelength, one of the most important GW parameters.

Zonal mean amplitudes for the three altitude intervals are in the range of 1.0 K to 2.5 K (Figure 6a). For the extratropics the mean amplitudes are lowest for the 20–25 km altitude range; i.e., the amplitudes increase with altitude. The increase of temperature amplitudes with altitude is a general feature due to the decrease of atmospheric density with height. This is much better visible in, e.g., SABER data covering the altitude range from about 20 km to 100 km [e.g., *Ern et al.*, 2011].

There is a strong meridional dependence of the temperature amplitude. For the lowest two altitude ranges the maximum amplitude is observed in the tropics with a second maximum in the Southern Hemisphere (SH) polar region. Only in the 30–35 km interval the amplitude exhibits the maximum in the SH high latitudes, and with additional maximum values in the tropics (north and south of the equator), in the Northern Hemisphere (NH) midlatitudes and high latitudes.

The higher amplitudes in the SH winter atmosphere compared with the NH summer months are due to the generally stronger wind conditions during winter especially in the SH polar vortex region. Caused by this atmospheric conditions, GWs propagate mostly opposite to the background wind and are Doppler shifted to longer vertical wavelengths. It should be noted that the period May to October 2006 is covering the SH winter

season and it is well known that the GW activity is higher during winter compared with the summer season. After *Preusse et al.* [2006] the saturated temperature amplitude $\hat{T}_{sat}$ can be expressed by

$$\hat{T}_{sat} = \frac{\bar{T} \cdot N^2 \cdot \lambda_z}{2\pi \cdot g} \tag{16}$$

As a consequence of equation (16) for longer vertical wavelengths λ_z, the maximum temperature amplitude $\hat{T}_{sat}$ before GW breaking occurs is enhanced [*Ern et al.*, 2011] and contributes to the mean amplitude maximum in SH middle and polar latitudes. The temperature amplitude maximum in the SH polar region during the time period investigated here is also present in HIRDLS data [*Yan et al.*, 2010] for the altitude range 22–32 km and in SABER data presented in the study from *Ern et al.* [2011].

Although there are very few studies about temperature amplitudes from RO data, the tropical maximum in the two lower altitude ranges is in agreement with previous potential energy (E_p) studies from *Tsuda et al.* [2000] or *de la Torre et al.* [2006] for the altitude interval between 20 km and 30 km. In contrast to the lower altitudes, for the 30–35 km altitude range the zonal mean maximum of the temperature amplitudes at the equator disappears and is split into two maximum values shifted northward and southward of the equator. This is accompanied by larger mean vertical wavelengths (Figure 6b) and in better agreement with SABER data at 30 km [*Ern et al.*, 2011]. We return to the tropical $\hat{T}$ maximum in connection with the tropical potential energy distribution below (section 7.3).

As discussed in section 3.1, the amplitudes from RO data are underestimated due to the limb sounding geometry and the RO retrieval assuming spherical symmetry of the refractivity field around the tangent point. This means that the zonal amplitudes presented here are supposed to be lower than the real amplitudes of the GW field.

7.2. Vertical Wavelength λ_z

From the dispersion relation (equation (2)) it follows that the intrinsic GW frequency $\hat{\omega}$ is directly related to the vertical wavelength λ_z or to the intrinsic phase speed $\hat{c}$:

$$\hat{c}^2 = (c - u_h)^2 = \frac{N^2 \cdot \lambda_z^2}{4\pi^2} \tag{17}$$

with c and u_h as the GW phase speed and the horizontal background wind, respectively. If the ground-based phase speed c converges to the background wind, the vertical wavelength λ_z approaches to zero and a critical level is reached.

From equation (16) and the momentum flux relation (equation (11)) it follows directly that the maximum (saturated) MF that can be carried by a GW is proportional to

$$\mathrm{MF}_{sat} \sim \frac{\lambda_z^3}{\lambda_h} \tag{18}$$

This means that short horizontal and/or large vertical wavelengths contribute much more to the maximum (saturated) momentum flux than longer (shorter) horizontal (vertical) wavelengths.

The zonal mean vertical wavelengths from RO data (Figure 6b) show a minimum of about 6.5–7.5 km in the tropics in all altitude intervals. The maximum (about 8.5–10 km) is observed in the SH extratropics and a second maximum in the NH midlatitudes with about 7.5–8.5 km.

The meridional distribution of the vertical wavelengths may indicate different processes for the generation of GWs. From equation (17) it follows that λ_z is proportional to $(c - u_h)$, and for simplification if one assumes stationary GWs ($c = 0$), λ_z increases directly with the background wind speed. Because our data analysis covers the SH winter (May to October 2006) with higher wind speeds in the midlatitude upper troposphere jet stream region compared to summer months and also with enhanced wind speed in the polar vortex region, the larger extratropical vertical wavelengths could be explained.

The tropical minimum and the SH polar maximum in λ_z was also observed by *Yan et al.* [2010] with HIRDLS data for the altitude interval between 22 km and 32 km during May to October 2006.

It should be noted again that the detection of vertical wavelengths from RO data is limited due to the altitude range covered here (20–40 km) and the vertical resolution of the RO technique (about 1 km in

the stratosphere). Vertical wavelengths less than 2 km and ultralong vertical wavelengths longer than 15–20 km are suppressed.

7.3. Potential Energy E_p

Beside the temperature amplitude and vertical wavelength, the potential energy E_p (equation (12)) can be calculated from a single temperature profile [*Tsuda et al.*, 2000]. E_p values based on RO data have been used for the detection of GW activity in various studies [e.g., *Tsuda et al.*, 2004; *de la Torre et al.*, 2006; *Baumgaertner and McDonald*, 2007; *Hei et al.*, 2008].

In Figure 6c the zonal mean potential energy for the three altitude intervals is revealed. The E_p behavior is very similar to the results for the temperature amplitudes (Figure 6a), but with larger variations between the different latitude bands. Considering the lower stratospheric E_p distibution (20–25 km and 25–30 km), a maximum in the tropics occurs [*Tsuda et al.*, 2000; *de la Torre et al.*, 2006]. The tropical E_p maximum is probably caused by a combination of planetary-scale Kelvin waves (KWs) and inertia-gravity waves. KWs have a characteristic eastward phase tilt with height, typical vertical wavelengths of about 4–10 km, and temperature amplitudes in the range of 2–4 K. The waves are often quasi-stationary near the tropopause but exhibit regular eastward propagation in the lower stratosphere [*Randel and Wu*, 2005]. Due to the presence of KWs, but also planetary-scale Rossby gravity waves in the equatorial lower stratosphere, they are probably not completely removed by the detrending method and are still present in the temperature fluctuations (equation (6)). Therefor, they could contribute to the enhanced tropical temperature amplitudes and potential energy distribution. For the effect of tropical planetary-scale waves we refer to section 8.3 where it is shown how this tropical E_p maximum is strongly reduced by a detrending using ERA-Interim data. On the other hand, *Alexander et al.* [2002] showed that GWs with short vertical wavelengths (Figure 6b) may include low intrinsic frequency $\hat{\omega}$ inertia-gravity waves and it can be also expected that these waves exhibit a peak in GW activity at the equator.

For the 30–35 km interval where vertical wavelengths are larger by about 1 km compared with the lower intervals (Figure 6b) the dominant equatorial E_p maximum vanishes and instead two symmetrical subtropical maximum values occur. This follows the same behavior of the zonal mean temperature amplitudes (Figure 6a) but much more pronounced in the meridional E_p distribution.

The generally enhanced stratospheric E_p values in the extratropics of the SH are related to higher GW activity during winter compared with the summer season. A similar pattern confirming our results is presented by *Zhang et al.* [2012] based on 8 years of SABER data (2002–2009), but for the altitude range between 21 km and 45 km. The SH E_p maximum around 60°S is observed at the edge of the polar vortex. Due to the enhanced background winds, Doppler shifting of waves to longer vertical wavelengths with larger amplitudes occurs in this area and is likely a major reason for the E_p maximum [*Baumgaertner and McDonald*, 2007]. This is consistent with the considerations about the temperature amplitudes in section 7.1.

7.4. Horizontal Wavelength λ_h

The determination of horizontal wavelengths is the main issue in this study, and the limitations due to the data sampling and combining measurements with different LOS directions were discussed in detail above. Generally, the horizontal wavelengths exhibit their maximum in the equatorial region and they decrease toward the poles (Figure 6d). This follows directly from equation (15) and is consistent with other studies [e.g., *Ern et al.*, 2004; *Preusse et al.*, 2006].

According to the dispersion relation, a maximum theoretical λ_h is given by $\hat{\omega}/f = 1$ which is shown in Figure 6d. It should be noted that for this calculation using equation (15), the observed values for N and λ_z were used. It is also evident that the extratropical λ_h values approach the theoretical λ_h with the ratio $\hat{\omega}/f = 1.9...2.0$. This is in agreement with the results from *Preusse et al.* [2006]. They found a convergence of extratropical λ_h for the ratio $\hat{\omega}/f = 1.8$ in the CRISTA data set. It is also evident from Figure 6d that zonal mean λ_h values agree for all different altitude intervals, i.e., there is no dominant change with altitude. For completeness the dotted black line in Figure 6d represents $4 \cdot \Delta x$ (twice the Nyquist wavelength) which serves as a lower boundary for the horizontal wavelength [*Ern et al.*, 2004]. The zonal mean λ_h values in the different altitude intervals are considerably larger than this lower limit and larger than the lower limit of horizontal wavelengths of about 100 km detectable with the RO technique [*Lange and Jacobi*, 2003].

Generally, the derived horizontal wavelengths based on triples of temperature profiles should better converge to the real horizontal wavelengths. As already discussed above, the apparent horizontal wavelengths derived

from two measurements are larger. This is demonstrated very clearly in the paper from *Alexander* [2015, Figure 3].

Compared to the previous studies from *Wang and Alexander* [2010] and *Faber et al.* [2013] using RO data for the determination of horizontal wavelengths, our data set is reduced and only zonal mean values are derived. The estimated horizontal wavelengths derived with the improved spatiotemporal data sampling are quite different. The horizontal wavelengths from *Wang and Alexander* [2010] vary between 1500 km in the polar regions and more than 4000 km in the tropics. Though *Faber et al.* [2013] introduced the improved method of temperature triples, the large spatiotemporal data sampling still leads to horizontal wavelengths with minimum values of 1500 km. Our approach with horizontal wavelengths in the range of about 700–800 km at high latitudes and 2000–2200 km in the equatorial region also based on triples of temperature profiles should be considered an improvement and extension of the *Faber et al.* [2013] study.

7.5. Momentum Flux (MF) and Wave Orientation α

Finally, the zonal mean momentum flux and the wave orientation is presented in Figures 6e and 6f. The MF is modulated by the variability of different wave parameters and directly proportional to the squared temperature amplitude and the ratio of vertical to horizontal wavelengths (equation (11)). The averaged MFs for the lower altitude intervals exhibit their maxima around 60°S at the edge of the SH polar vortex: about 10.5 mPa between 20 and 25 km and about 6 mPa between 25 and 30 km. Secondary maxima values for the 20–25 km interval of about 4.5 mPa in the tropics and of about 5 mPa in the NH subtropics and midlatitudes are found (Figure 6e). The tropical maximum nearly vanishes between 25 and 30 km but is still present in the NH midlatitudes (about 4 mPa). For the upper altitude interval (30–35 km) there is only a moderate latitudinal variation with only small enhanced absolute MF values around 60°S and in the NH midlatitudes; however, the relative variations are similarly strong as for the other altitudes. It is evident that the momentum flux decreases clearly with height. Because the momentum flux is proportional to the potential energy and the ratio of vertical to horizontal wavelengths (equation (13)), the zonal mean MF does not have to follow the course of the potential energy. This is mainly relevant for the equatorial region where E_p clearly peaks for averages between 20–25 km and 25–30 km, but not with this magnitude for the MF (Figures 6c and 6e).

Generally, our MF results for the 20–25 km interval are in good agreement with the momentum fluxes estimated from *Alexander* [2015, Figure 2] for the altitude interval between 17 km and 22 km based on the combined HIRDLS and COSMIC data. Both *Alexander* [2015] and we in our study use triples of temperature fluctuation profiles to estimate the horizontal wavelength in contrast to previous studies based on pairs of measurements [e.g., *Ern et al.*, 2004; *Alexander et al.*, 2008; *Ern et al.*, 2011]. We exclude here the results from *Wang and Alexander* [2010] and *Faber et al.* [2013] because of their insufficient data sampling. Although *Alexander* [2015] utilizes a combined data set from HIRDLS and COSMIC data, the momentum flux results with our study agree not only qualitatively but also quantitatively and can be considered as an independent assessment.

For a comparison of our MF results with other observational data in the lower stratosphere based on profile pairs we use the study from *Geller et al.* [2013] (their right side of Figure 1) containing zonal mean MF data for July 2006. The authors present observational data from SABER ($\geq$ 30 km height) and two HIRDLS ($\geq$20 km height) data sets based on different data processing for the estimation of the momentum flux. For the HIRDLS1 MF the approach from *Alexander et al.* [2008] is used based on a cospectral analysis of the profile pairs. The HIRDLS2 and SABER momentum fluxes followed the approach from *Ern et al.* [2011] that analyzes each profile separately and considers the results only if the dominant vertical wave structure is present in both profiles. The latter method is similar to our approach (section 6).

Figure 7 shows the zonal mean momentum flux from RO similar to Figure 6e but for June–August 2006 only. The differences to the complete time interval (May to October 2006) are marginal for the SH, but for the NH subtropics the MF is larger. This is plausible because of the higher GW activity in association with the poleward shift of the Intertropical Convergence Zone during summer.

If we compare the zonal mean MF values from Figure 7 with the Geller et al. study, it is evident that the MF at 20 km and 30 km agrees only qualitatively in the SH polar vortex region and in the NH subtropics. The SH MF maximum is present in the HIRDLS and SABER data sets, but the remaining latitudinal structure is somewhat different than in Figure 7. For a detailed discussion of the differences between the HIRDLS1 and HIRDLS2

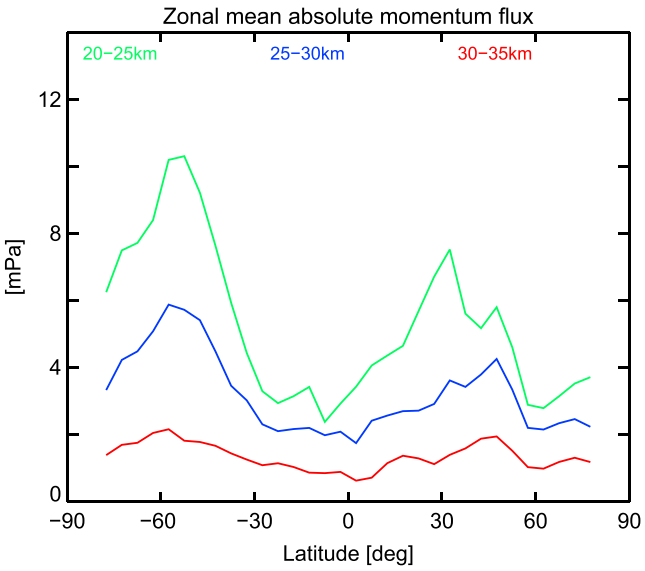

Figure 7. Zonal mean momentum flux (MF) for different altitude intervals based on the time period June to August 2006 and horizontal detrending with RO data (similar to Figure 6e but with different time interval).

data sets we refer to *Geller et al.* [2013] and focus here to a comparison of our MF values to the presented observational values.

In Table 1 the SABER, HIRDLS, and RO MF data are quantitatively compared for selected latitude ranges. The values are roughly estimates from Figure 1 in *Geller et al.* [2013] for the SABER and HIRLDS data and from Figure 7 for the RO values. It should be noted that the SABER and HIRDLS values are from fixed altitudes at 20 km and 30 km, but the RO values are averages over 5 km, which means that for the 20 km altitude level the RO data (20–25 km average) are underestimated, whereas for the 30 km level the RO values (25–30 km average) are overestimated compared to SABER and HIRDLS because of the general decrease of the MF with height. Further, the time intervals for the RO (June–August) and SABER/HIRDLS (July only) data are also slightly different. Therefore, Table 1 presents only a roughly quantitative comparison but allows to highlight some general differences.

For the SH MF maximum in the polar vortex region the RO values for both altitudes are between the HIRDLS1 and HIRDLS2 data, i.e., at the same magnitude. The RO momentum flux of the remaining latitudes exhibits much larger values with a factor up to 10 between HIRDLS1 and RO for the 40°N–50°N interval. The main difference for the estimation of MF between the SABER and HIRDLS and the RO data is the usage of temperature pairs and triples for the estimation of the horizontal wavelengths. The consequences are shorter λ_h values and larger MF with the application of the "triple" method. It is remarkable that for this rough comparison the differences in zonal mean momentum flux are small in the MF peak region of the SH around 60°S. For all other latitude bands the differences are much larger. On the other hand, one should keep in mind that in Table 1 only roughly the same altitude and time intervals are compared. In addition, there might be also differences in the processing schema (as discussed in *Geller et al.* [2013] for the HIRDLS1/HIRDLS2 data) that are not considered here. Therefore, it is highly recommended to compare the processing steps for the derivation of satellite-based momentum fluxes in future validation studies.

Table 1. Approximated Momentum Fluxes for Different Latitude and Altitude Ranges[a]

	50°–60°S (mPa)	10°N–10°S (mPa)	20°–30°N (mPa)	40°–50°N (mPa)
		20 km		
HIRDLS1	17	0.5	1	0.5
HIRDLS2	8	1	2	1.5
SABER				
RO	10.5	3–4	5–6	5
		30 km		
HIRDLS1	6	<0.5	0.7	<0.5
HIRDLS2	6.5	0.5	1	0.5
SABER	4.5	1	1–1.5	0.6
RO	6	2	3	4

[a]The HIRDLS and SABER values are roughly estimates from Figure 1 in *Geller et al.* [2013], the RO values from Figure 7. SABER data are not available below 30 km. The RO data are averages between 20–25 km (upper part of the table) and 25–30 km (lower part of the table).

As demonstrated by *Faber et al.* [2013] and recently by *Alexander* [2015], a larger spatial sampling pattern leads to larger (lower) horizontal wavelengths (momentum fluxes), whereas the mean MF variation between a 20 min/200 km and a 20 min/600 km limit differs by about 20% [*Alexander*, 2015].

For completeness Figure 6f presents the mean orientation of the GWs. Because the direction of wave propagation can only

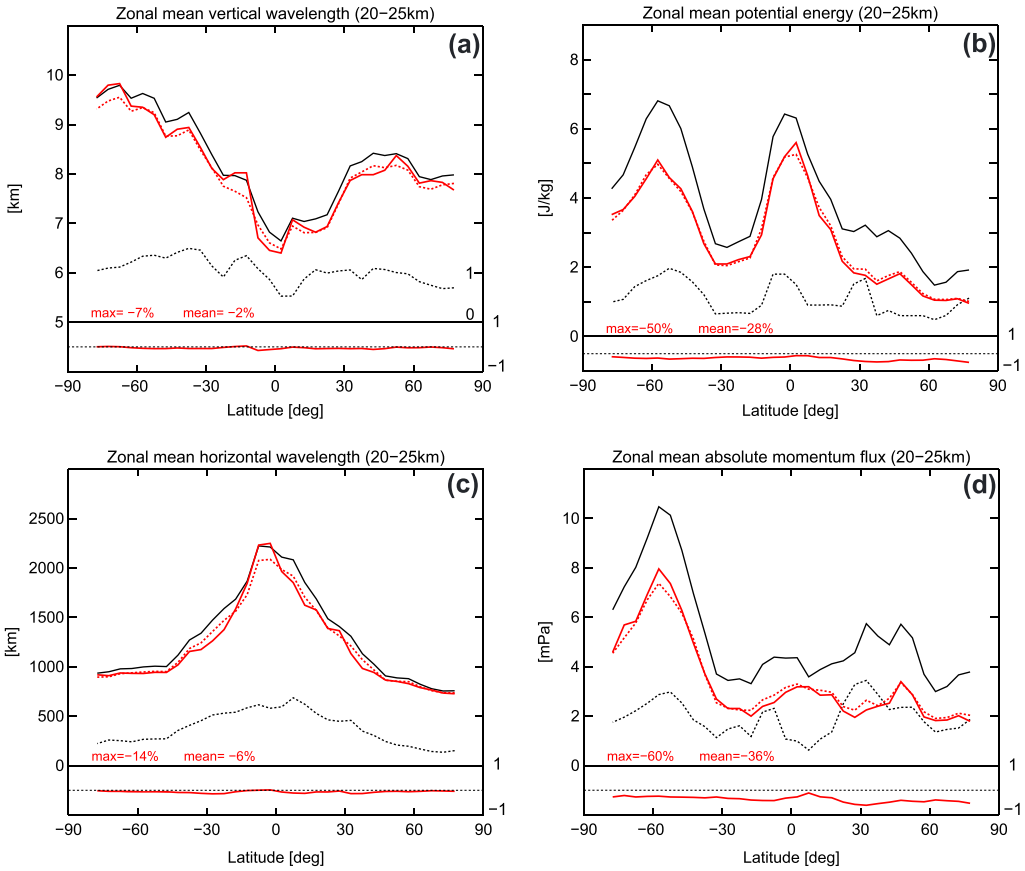

Figure 8. (a) Zonal mean vertical wavelength λ_z between 20 km and 25 km based on the time period May to October 2006 and horizontal detrending with RO data (solid black line). The dotted black line denotes the 1σ standard deviation, the solid red line denotes the median, and the red dotted line denotes the geometric mean, respectively. In the lower part the relative difference (median − mean)/mean is shown with the absolute maximum and mean value over all latitudes. The *y* axis for the standard deviation is on the right starting with 0 km. (b) For the potential energy E_p. (c) For the horizontal wavelength λ_h. (d) The absolute momentum flux (MF).

be determined with a 180° ambiguity, both units on the left and right could be applied. One can clearly see that the prevailing orientation for all altitude intervals considered here is between 60° and 110° or between 240° and 290° (counted from north = 0°).

8. Error Discussion

The results in Figure 6 refer to mean values, but no standard deviation was discussed. Further, not all GW parameters follow a Gaussian distribution, which means that the geometric mean and also the median could be a better parameter to characterize the distribution. These aspects will be pointed out below. We have already discussed the data sampling that has influence on the final momentum flux. We will quantify this for selected GW parameters, and finally, different detrending methods and their effects on different GW parameters are investigated.

8.1. Statistical Parameter

In this section statistical characteristics of selected GW parameters are discussed. We refer to the vertical and horizontal wavelength, the potential energy, and the momentum flux for the altitude range between 20 km and 25 km. In Figure 8 the mean (solid black line) and the standard deviation (black dotted line) for each parameter are presented. The mean values are identical with the green solid lines in Figure 6.

For the vertical wavelength λ_z the standard deviation varies between 0.5 km in the equatorial region and about 1.5 km in the SH subtropics and midlatitudes (Figure 8a). The higher variability on the SH can be explained by the winter season with stronger and variable wind conditions. This interpretation is also valid

Table 2. Relative Differences Between Arithmetic Mean and Median Values (Median − Mean)/Mean for Different Gravity Wave Parameters and Altitude Intervals[a]

	Global Mean Difference (%)	Maximum (%)	Latitude of Maximum (deg)
	20–25 km		
Temperature amplitude	−9	−17	77.5
Vertical wavelength	−2	−7	−7.5
Potential energy	−28	−50	77.5
Horizontal wavelength	−6	−14	−27.5
Absolute momentum flux	−36	−60	32.5
	25–30 km		
Temperature amplitude	−7	−17	37.5
Vertical wavelength	−2	−5	−57.5
Potential energy	−22	−50	42.5
Horizontal wavelength	−5	−16	−22.5
Absolute momentum flux	−31	−49	37.5
	30–35 km		
Temperature amplitude	−8	−20	77.5
Vertical wavelength	−1	−4	−57.5
Potential energy	−25	−51	42.5
Horizontal wavelength	−6	−19	12.5
Absolute momentum flux	−33	−51	77.5

[a]The latitude is the center of a 5° interval.

for the potential energy (Figure 8b). The E_p standard deviation exhibits maximum values (1.8 J/kg) where the mean is also peaked. The northern summer hemisphere exhibits only small standard deviation with values less than 1 J/kg. For the horizontal wavelength distribution the standard deviation is about 200–250 km in high latitudes and about 500 km in the equatorial region; i.e., the spread is with values of about 25–30% around the mean (Figure 8c). Similar to the vertical wavelength and potential energy, the standard deviation for λ_h is larger on the southern winter hemisphere. The standard deviation for the momentum flux shows different behavior with maximum values around 3 mPa (by mean values around 5.5 mPs) in the NH subtropics, i.e., on the summer hemisphere (Figure 8d). This could be related to changing GW generation conditions in the vicinity of the subtropical jet during summer. On the other hand, the small MF standard deviation on the SH polar vortex region denotes a relatively stable mean momentum flux.

As discussed by *Baumgaertner and McDonald* [2007] and *Alexander et al.* [2015], the potential energy distribution has a more lognormal than a Gaussian distribution. For this reason in Figure 8 also the geometric mean (dotted red line) and the median (solid red line) are presented which differ only slightly from each other for all GW parameters considered here. The differences between the arithmetic mean and the median are much larger for some parameter. For the vertical and horizontal wavelengths (Figures 8a and 8c) the deviations between mean and median are small with only 2% on global average (maximum 7%) for λ_z and 6% on global average (maximum 14%) for λ_h. For the potential energy and the momentum flux the differences are much larger; i.e., the according distributions do not follow a Gaussian distribution. For E_p a global averaged difference between mean and median of 28% (maximum 50%) occurs, whereas the values for MF are slightly larger: global average of 36% with a maximum difference of 60%. In all cases the median is less than the mean value. The relative differences (median − mean)/mean with respect to the mean values are plotted in the lower part of each figure.

For the MF median distribution also a SH polar vortex maximum is present, but in the tropics a shift from the arithmetic mean peak south of the equator toward a median peak north of the equator occurs. In Table 2 the differences between mean and median values and the maximum value with the according latitude band for all GW parameter are given.

8.2. Comparison of GW Parameter With Different Data Sampling

In section 3 we have discussed in detail possible error sources for the phase shift determination between two adjacent temperature fluctuation profiles by combining measurements with different LOS and temporal and spatial data sampling. As a consequence, we introduced beside the maximum time interval of 15 min and maximum sampling distance of 250 km an additional lower sampling distance which we defined latitude dependent (equation (4)).

For the quantification of different sampling setups on GW parameter two different cases were considered and the results are given in Figure 9 for the mean vertical and horizontal wavelengths, the potential energy, and the momentum flux in the altitude range between 20 km and 25 km: case 1 with minimum sampling

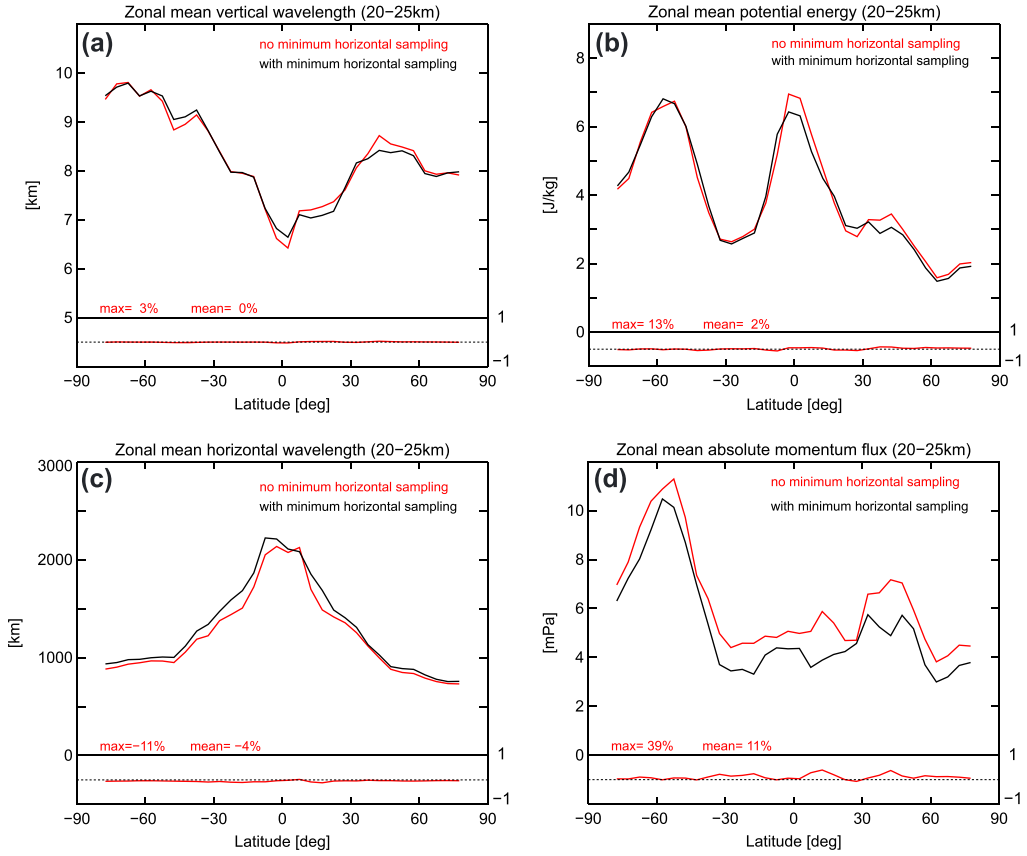

Figure 9. (a) Zonal mean vertical wavelength λ_z between 20 km and 25 km based on the time period May to October 2006 and horizontal detrending with RO data for two different cases. (C1) with minimum sampling distance criterion (solid black line); (C2) no minimum sampling distance criterion (solid red line). In the lower part the relative difference (C2−C1)/C1 is shown with the absolute maximum and mean value over all latitudes. (b) For the potential energy E_p. (c) For the horizontal wavelength λ_h. (d) For the absolute momentum flux (MF).

distance (equation (4)) criterion (solid black line) and case 2 with no minimum sampling distance criterion (solid red line).

In the lower part of Figure 9 the relative differences between case 1 and case 2 with respect to case 1 (C2−C1)/C1 are shown with the absolute maximum and mean value over all latitudes.

The application of the minimum sampling distance criterion is very important, but not for each GW parameter. For the vertical wavelength λ_z and the potential energy E_p that can be derived from a single profile a minimum sampling distance criterion is of course irrelevant. This is demonstrated by the very good agreement between the black (minimum horizontal criterion applied) and red (no minimum horizontal criterion) lines in Figures 9a and 9b. However, in the equatorial region and the NH subtropics (30°N−40°N) larger differences occur with higher E_p values if the minimum sampling distance criterion is not applied.

For the horizontal wavelength distribution (Figure 9c) the application of the minimum sampling criterion leads to larger horizontal wavelengths and as a result to smaller momentum fluxes compared to the results when the criterion is not applied (Figure 9d). As discussed above, an insufficient data sampling may lead to random distributed phase differences and horizontal wavelengths that are estimated too short for this cases [*Ern et al.*, 2004]. In total, the global averaged difference for λ_h between the two cases (minimum distance criterion applied versus not applied) is about 4% (maximum 11%) with lower values if the sampling distance criterion is not considered (Figure 9c). The effect is relatively constant for all latitude bands but much more larger for the momentum flux (Figure 9d). Zonal mean MF values are up to 39% larger (global average 11%) if the minimum sampling distance criterion is not applied.

Table 3. Relative Difference Between Gravity Wave Parameters Derived With (*Y*) and Without (*N*) the Minimum Sampling Criterion [(*N* − *Y*)/*Y*][a]

	Global Mean Difference (%)	Maximum (%)	Latitude of Maximum (deg)
	20–25 km		
Temperature amplitude	0	−6	−7.5
Vertical wavelength	0	3	42.5
Potential energy	2	13	37.5
Horizontal wavelength	−4	−11	17.5
Absolute momentum flux	11	39	12.5
	25–30 km		
Temperature amplitude	1	7	42.5
Vertical wavelength	0	4	12.5
Potential energy	3	16	42.5
Horizontal wavelength	−4	−16	−17.5
Absolute momentum flux	15	46	12.5
	30–35 km		
Temperature amplitude	2	11	42.5
Vertical wavelength	0	2	12.5
Potential energy	5	28	42.5
Horizontal wavelength	−5	−15	17.5
Absolute momentum flux	17	41	42.5

[a]The latitude is the center of a 5° interval.

In Table 3 the differences between the processing with and without the application of the minimum sampling distance are presented for all GW parameters and also for the 25–30 km and 30–35 km altitude ranges. The differences increase with altitude with maximum deviations for the MF of 46% (25–30 km) in the 12.5°N latitude band.

8.3. GW Parameter With Different Detrending Methods

One of the basic requirements in GW analysis is the separation of GW and large-scale non-GW components in the observed temperature profiles (equation (6)). This is called detrending and is obligatory for each GW observing method. The applied detrending approach (section 5) depends on the available data density, and the qualitative and quantitative distribution of GW parameter depends on the chosen detrending method. For the potential energy *John and Kumar* [2013] found significant differences between a horizontal and vertical detrending. The reason is that with a vertical detrending a large part of planetary waves is still present in the temperature fluctuation and not assigned to the temperature background.

For the horizontal detrending described in section 5 the data density of the used data set must be suitable to construct best daily climatologies based on a sufficient number of profiles per latitude-longitude bin. For RO data this is not continuously the case and even climatologies based on averages over 3 days are sometimes difficult to derive because of the nonuniform distribution of the RO data. On the other hand, significant climatologies are the basis for the horizontal detrending approach. We use in this study 3 day RO climatologies and introduce in addition a novel method of horizontal detrending of RO data with ERA-Interim temperatures based on 1 day climatologies. Although some GWs are resolved in ECMWF data [*Schroeder et al.*, 2009], their signal will be reduced due to averaging over 1 day. For a maximum removal of the remaining GWs in the daily ERA-Interim climatology zonal wave numbers 0–6 as a function of longitude are constructed using the *S* transform similar to the RO data (section 5).

By the interpretation of the results with different detrending methods, one should keep in mind that the temperature fluctuation profiles based on vertical detrending still contain large-scale contributions of planetary and/or other waves. The horizontal detrending removes most of the large-scale components in the fluctuation profiles, but for the detrending with the RO data based on 3 day climatologies traveling planetary wave components may still be included.

Figure 10 shows the zonal mean vertical wavelength, horizontal wavelength, potential energy, and absolute momentum flux averaged between 20 km and 25 km and based on the three detrending methods investigated here: Method 1: horizontal detrending using RO (black), Method 2: horizontal detrending using ERA-Interim (blue), and Method 3: vertical detrending (red).

In the lower parts of Figure 10 the relative differences between Method 1 (M1) and Method 2 (M2) and between Method 1 and Method 3 (M3) are presented. For each GW parameter considered here the differences between the two types of horizontal detrending (M1 and M2) are much smaller compared to the vertical detrending method M3.

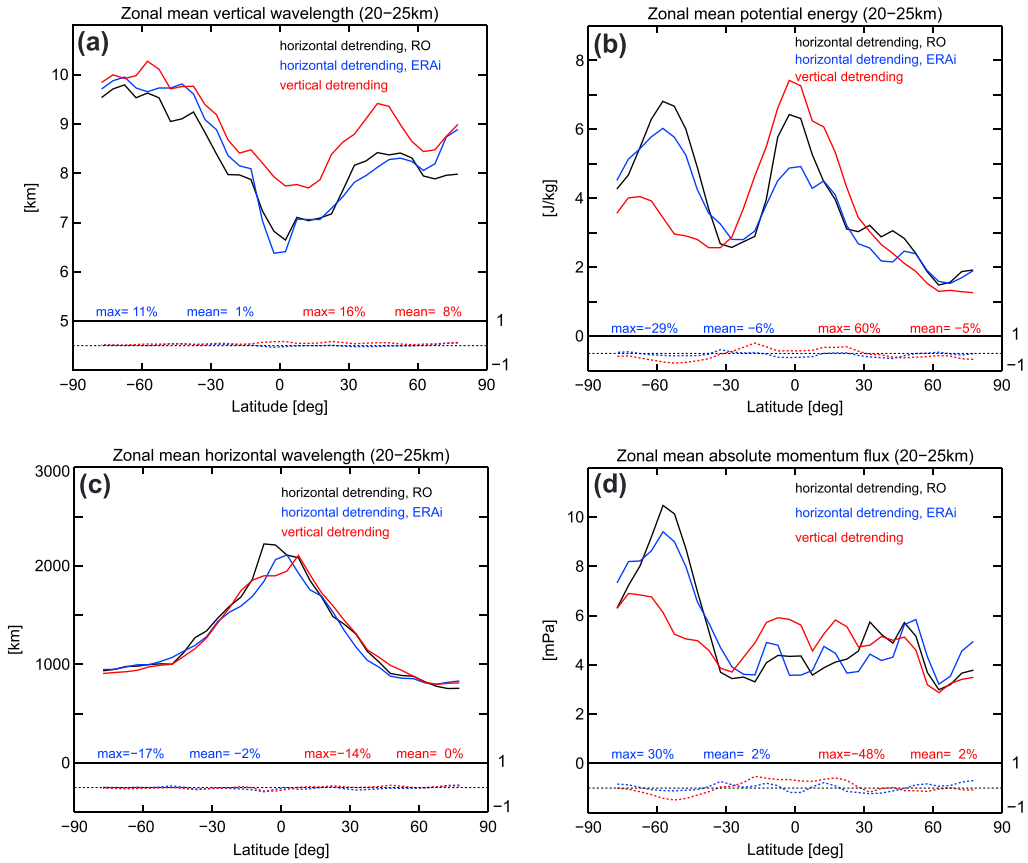

Figure 10. (a) Zonal mean vertical wavelength λ_z between 20 km and 25 km based on the time period May to October 2006 for three different detrending methods M1–M3. (M1) solid black line: horizontal detrending using RO data, (M2) solid blue line: horizontal detrending using ERA-Interim data, and (M3) solid red line: vertical detrending. In the lower part the relative differences (M2 − M1)/M1 (dotted blue line) and (M3 − M1)/M1 (dotted red line) are shown with the absolute maximum values over all latitudes. (b) For the potential energy E_p. (c) For the horizontal wavelength λ_h. (d) For the absolute momentum flux (MF).

For the vertical wavelength λ_z (Figure 10a) all the methods agree qualitatively, but the horizontal methods M1 and M2 coincide much better especially in the NH. λ_z values based on method M3 are generally larger up to 1 km, and the minimum vertical wavelengths observed with M1 and M2 near the equator are shifted northward for method M3. The vertical detrending with the band-pass filter between 2 and 15 km may give smoother temperature fluctuation profiles compared to the horizontal detrending with the result that the wavelet analysis originates larger vertical wavelengths for the vertical detrended temperature fluctuations. The global averaged mean relative difference between M1 and M2 is about 1% (maximum 11%), and between methods M1 and M3 the difference is enhanced (8%) with a maximum of about 16%. In Table 4 all differences between all methods for all GW parameter are listed for reference.

The comparison of the potential energy derived with the different detrending methods shows the effect among the methods most clearly (Figure 10b). Both horizontal detrending methods M1 and M2 agree very good with three exceptions. The first is in the equatorial region and the other are the midlatitudes of both hemispheres (SH between 40° and 60° and NH between 30° and 50°). In these regions E_p based on method M1 exhibits larger values than with method M2. The differences are between 0.5 and 1 J/kg. A reason for the enhanced E_p values with the M1 method is supposed to be due to the larger time interval for the generation of the RO climatologies and therefore a inclusion of more traveling planetary waves in the temperature fluctuations.

Generally, the zonal mean potential energy values between 20 and 25 km are largest with vertical detrending compared to horizontal detrending in the tropics (30°N–30°S). This is supposed to be due to large parts of Kelvin and/or Rossby gravity waves that are still included in the temperature fluctuations derived with vertical

Table 4. Relative Differences Between Gravity Wave Parameters Derived With Different Detrending Methods[a]

	(M2 – M1)/M1 (%)		(M3 – M1)/M1 (%)	
	Mean	Maximum	Mean	Maximum
		20–25 km		
Temperature amplitude	0	12	–2	–29
Vertical wavelength	1	11	8	16
Potential energy	–6	–29	–5	60
Horizontal wavelength	–2	–17	0	–14
Absolute momentum flux	2	30	2	–48
		25–30 km		
Temperature amplitude	0	–18	–3	–21
Vertical wavelength	1	15	12	30
Potential energy	–2	–30	–6	–44
Horizontal wavelength	–2	14	–4	–26
Absolute momentum flux	6	31	15	90
		30–35 km		
Temperature amplitude	4	16	4	19
Vertical wavelength	0	7	9	31
Potential energy	4	33	8	46
Horizontal wavelength	–3	–20	–4	–25
Absolute momentum flux	12	56	26	107

[a]M1: horizontal detrending using RO data, M2: horizontal detrending using ERA-Interim data, and M3: vertical detrending.

detrending [*de la Torre et al.*, 2006; *John and Kumar*, 2013]. From Figure 10b it follows that the horizontal detrending with ERA-Interim data removes best the large-scale wave contributions leading to an important reduction of the GW activity in the equatorial region compared to previous studies [e.g., *Tsuda et al.*, 2000; *de la Torre et al.*, 2006].

However, in the extratropics of both hemispheres the zonal mean potential energy from vertical detrending (M3) is smaller compared with the horizontal methods (M1 and M2). The effect is maximized in the SH by about 50%. This means that the vertical detrending leads to an underestimation (with respect to methods M1 and M2) of GW activity in a region that is expected to have enhanced activity because the time period covered here includes the complete SH winter season where wave activity is generally enhanced. Because the zonal mean temperature amplitudes in that region (30°S–60°S) show a similar course than the zonal E_p distribution in Figure 10b (not shown here), it is supposed that the vertical band-pass filter applied here results in smaller temperature fluctuations compared with the horizontal detrending. Another effect that reduces E_p during SH winter by method M3 follows directly from the band-pass filter allowing only GWs with λ_z<15 km. Because gravity wave vertical wavelengths can become quite large by Doppler shifting in the strong polar vortex winds, the reduction of E_p by method M3 is plausible. The vertical detrended profiles exhibit the E_p peak farther south at about 75°S which is in agreement with, e.g., *de la Torre et al.* [2006] who have also applied band-pass filter for vertical detrending.

In the lower part of Figure 10b the relative E_p differences of the methods M2 and M3 to the horizontal detrending using RO data (M1) are presented. The global averaged differences between methods M1 and M2 are about 6% (maximum 29% in the equatorial region), whereas the differences between methods M1 and M3 are larger with a maximum deviation of 60%.

The differences in the zonal mean horizontal wavelengths (Figure 10c) due to the different detrending methods are small in the extratropics. Only in the equatorial region relative differences between 14% and 17% occur. On global average there is no difference between the horizontal detrending with RO data (M1) and the vertical detrending (M3). The zonal mean λ_h values between both horizontal detrending methods M1 and M2 vary globally by 2%. The most important parameter for the λ_h determination is the phase shift between the adjacent temperature fluctuation profiles (equation (5)). This means that the phase shift between the profile pairs is not much affected by the detrending method itself.

Finally, Figure 10d presents the zonal mean momentum flux derived with different detrending methods. It is evident that the MF estimated on the basis of horizontal detrending agrees very good among each other with a global mean relative difference of 2%. Although the global mean difference between methods M1 and M3 is also only 2%, the differences in some latitudes are much larger (up to 48%) than between methods M1 and M2. The MF based on the vertical detrending is lower than for horizontal detrending in the extratropics but larger in the tropics. This is nearly similar to the potential energy, whereas the momentum flux also depends on the ratio of vertical to horizontal wavelengths. This is consistent with the results for the potential energy.

All detending methods exhibit the MF maximum on the SH polar vortex region but shifted some degrees south for the vertical detrending.

The tropical and extratropical differences in the MF for the horizontal and vertical detrending methods can be explained by the proportionality of the MF to the ratio of vertical to horizontal wavelengths and the potential energy (equation (13)). While the zonal mean horizontal wavelengths are nearly independent from the detrending method (Figure 10c), mainly, the λ_z and E_p distributions determine the differences in MF. The vertical wavelengths are generally larger with the vertical detrending (Figure 10a), and in combination with large potential energy in the tropics (Figure 10b) the higher momentum flux in the tropics compared to horizontal detrending can be explained. Although the vertical wavelengths with method M3 are higher than with M1 and M2, this effect is compensated by lower E_p values in the extratropics leading to lower momentum fluxes based on vertical detrending compared with horizontal detrending in the extratropics.

9. Conclusions

The focus on this paper is on the determination of momentum fluxes in the lower and middle stratosphere (20–40 km) and the discussion of mean GW parameters for three altitude intervals (20–25 km, 25–30 km, and 30–35 km). The key goal is the determination of real horizontal wavelengths.

Because of the generally shorter horizontal wavelengths derived with the application of temperature profile triples in comparison to apparent horizontal wavelengths derived between adjacent temperature profiles in former studies, we estimate absolute momentum fluxes that are remarkably larger, for example, in comparison to the study of *Geller et al.* [2013]. This is the most important result of our study with implications for the parametrization of GWs in global circulation models. Because similar results for the global distribution of momentum fluxes are presented by *Alexander* [2015] from a combination of HIRDLS and COSMIC data in 2007, our study can be considered as an independent validation supporting the recently derived results from *Alexander* [2015].

On the other hand, due to the strong data sampling limits that are necessary for a realistic estimation of momentum fluxes, our study is limited to a very short time period in 2006 to the beginning of the COSMIC mission because of the availability of a sufficient number of measured triples of nearby temperature profiles. Nevertheless, with this study we could demonstrate that also from radio occultation data if the data sampling is correct, an estimation of absolute stratospheric momentum fluxes is possible. This is a contribution to and an extension of momentum flux climatologies derived from other satellites (CRISTA, SABER, or HIRDLS). Of course, a determination of net momentum fluxes is also not possible with RO data.

The potential of the RO data for future momentum flux estimations will improve if the COSMIC-2 mission is fully operating. Together with other RO missions (e.g., Metop) and the possibility to receive in addition to the GPS signals also the Russian Global Navigation Satellite System and/or the Chinese BaiDo system by a new generation of space-based GNSS receiver, the data density will improve significantly. GNSS stands for Global Navigation Satellite Systems and is not limited to GPS only as in the past.

The other main result of this study shows that different detrending methods give different results of GW parameters and supports results of previous studies but here focused on the momentum flux and based on a detailed quantitative analysis. Because the differences in nearly all GW parameters (mainly MF) are smaller between both horizontal detrending methods (even if they are based on different data sets) compared with vertical detrending, it is strongly recommended to perform horizontal detrending for the removal of large-scale planetary wave components. If the RO data density is not sufficient for horizontal detrending, the application of model data is an alternative as demonstrated here with ERA-Interim data.

Acknowledgments
The authors would like to thank the anonymous reviewers for their helpful comments and suggestions that have improved the manuscript. We would also like to thank the FORMOSAT3/COSMIC teams in Taiwan and the U.S. for maintaining the mission, processing the radio occultation data, and making them freely available for the scientific user community (http://cdaac-www.cosmic.ucar.edu/cdaac/products.html). The study has been supported by the German Federal Ministry of Education and Research (BMBF) under grant 01DN14001 and by CONICET under grants CONICET PIP 11220120100034 and ANPCYT PICT 2013-1097. P. Alexander and A. de la Torre are members of CONICET.

References

Allen, S. J., and R. A. Vincent (1995), Gravity wave activity in the lower atmosphere: Seasonal and latitudinal variations, *J. Geophys. Res.*, *100*, 1327–1350.

Anthes, R. A. (2011), Exploring Earth's atmosphere with radio occultation: Contributions to weather, climate and space weather, *Atmos. Meas. Tech.*, *4*, 1077–1103, doi:10.5194/amt-4-1077-2011.

Anthes, R. A., et al. (2008), The COSMIC/Formosat-3 mission: Early results, *Am. Meteorol. Soc.*, *89*, 313–333, doi:10.1175/BAMS-89-3-313.

Alexander, M. J., et al. (2002), On the latitudinal variations observed in gravity waves with short vertical wavelengths, *J. Atmos. Sci.*, *59*, 1394–1404.

Alexander, M. J., et al. (2008), Global estimates of gravity wave momentum flux from High Resolution Dynamics Limb Sounder observations, *J. Geophys. Res.*, *113*, D15S18, doi:10.1029/2007JD008807.
Alexander, M. J., et al. (2010), Recent developments in gravity-wave effects in climate models and the global distribution of gravity-wave momentum flux from observations and models, *Q. J. R. Meteorol. Soc.*, *136*, 1103–1124, doi:10.1002/qj.637.
Alexander, M. J. (2015), Global and seasonal variations in three-dimensional gravity wave momentum flux from satellite limb-sounding temperatures, *Geophys. Res. Lett.*, *42*, 6860–6867, doi:10.1002/2015GL065234.
Alexander, P., et al. (2008), Interpretation of gravity wave signatures in GPS radio occultations, *J. Geophys. Res.*, *113*, D16117, doi:10.1029/2007JD009390.
Alexander, P., et al. (2015), Distribution functions and statistical parameters that may be used to characterize limb sounders gravity wave climatologies in the stratosphere, *Adv. Space Res.*, *56*, 619–633, doi:10.1016/j.asr.2015.05.007.
Baumgaertner, A. J. G., and A. J. McDonald (2007), A gravity wave climatology for Antarctica compiled from Challenging Minisatellite Payload/Global Positioning System (CHAMP/GPS) radio occultations, *J. Geophys. Res.*, *112*, D05103, doi:10.1029/2006JD007504.
Dee, D. P., et al. (2011), The ERA-Interim reanalysis: Configuration and performance of the data assimilation system, *Q. J. R. Meteorol. Soc.*, *137*, 553–597, doi:10.1002/qj.828.
de la Torre, A., et al. (2006), A global analysis of wave potential energy in the lower stratosphere derived from 5 years of GPS radio occultation data with CHAMP, *Geophys. Res. Lett.*, *33*, L24809, doi:10.1029/2006GL027696.
Ern, M., et al. (2004), Absolute values of gravity wave momentum flux derived from satellite data, *J. Geophys. Res.*, *109*, D20103, doi:10.1029/2004JD004752.
Ern, M., and P. Preusse (2009), Quantification of the contribution of equatorial Kelvin waves to the QBO wind reversal in the stratosphere, *Geophys. Res. Lett.*, *36*, L21801, doi:10.1029/2009GL040493.
Ern, M., et al. (2011), Implications for atmospheric dynamics derived from global observations of gravity wave momentum flux in stratosphere and mesosphere, *J. Geophys. Res.*, *116*, D19107, doi:10.1029/2011JD015821.
Faber, A., et al. (2013), On the determination of gravity wave momentum flux from GPS radio occultation data, *Atmos. Meas. Tech.*, *6*, 3169–3180, doi:10.5194/amt-6-3169-2013.
Fritts, D. C., and M. J. Alexander (2003), Gravity wave dynamics and effects in the middle atmosphere, *Rev. Geophys.*, *41*(1), 1003, doi:10.1029/2001RG000106.
Fritts, D. C., et al. (2006), Mean and variable forcing of the middle atmosphere by gravity waves, *J. Atmos. Sol. Terr. Phys.*, *68*, 247–265, doi:10.1016/j.jastp.2005.04.010.
Froehlich, K., et al. (2007), The global distribution of gravity wave energy in the lower stratosphere derived from GPS data and gravity wave modelling: Attempt and challenges, *J. Atmos. Sol. Terr. Phys.*, *69*, 2238–2248, doi:10.1016/j.jastp.2007.07.005.
Geller, M. A., et al. (2013), A comparison between gravity wave momentum fluxes in observations and climate models, *26*, 6383–6405, doi:10.1175/JCLI-D-12-00545.1.
Gille, J., et al. (2008), High Resolution Dynamics Limb Sounder: Experiment overview, recovery, and validation of initial temperature data, *J. Geophys. Res.*, *113*, D16S43, doi:10.1029/2007JD008824.
Hei, H., et al. (2008), Characteristics of atmospheric gravity wave activity in the polar regions revealed by GPS radio occultation data with CHAMP, *J. Geophys. Res.*, *113*, D04107, doi:10.1029/2007JD008938.
Heale, C. J., et al. (2014), Thermospheric dissipation of upward propagating gravity wave packets, *J. Geophys. Res. Space Physics*, *119*, 3857–3872, doi:10.1002/2013JA019387.
John, S. R., and K. K. Kumar (2013), A discussion on the methods of extracting gravity wave perturbations from space-based measurements, *Geophys. Res. Lett.*, *40*, 2406–2410, doi:10.1002/grl.50451.
Kursinski, E. R., et al. (1997), Observing Earth's atmosphere with radio occultation measurements using the Global Positioning System, *J. Geophys. Res.*, *102*, 23,429–23,465.
Lange, M., and C. Jacobi (2003), Analysis of gravity waves from radio occultation measurements, in *First CHAMP Mission Results for Gravity, Magnetic and Atmospheric Studies*, edited by C. Reigber, H. Lühr, and P. Schwintzer, pp. 479–484, Springer, Berlin.
Lindzen, R. S., and J. R. Holton (1968), A theory of the Quasi-Biennial Oscillation, *J. Atmos. Sci.*, *25*, 1095–1107.
Marquardt, C., and S. B. Healy (2005), Measurement noise and stratospheric gravity wave characteristics obtained from GPS occultation data, *J. Meteorol. Soc. Jpn.*, *83*, 417–428.
Nappo, C. J. (2002), *An Introduction to Atmospheric Gravity Waves, Intern. Geophys. Ser.*, vol. 85, 276 pp., Academic Press, San Diego, Calif.
Offermann, D., et al. (1999), Cryogenic Infrared Spectrometers and Telescopes for the Atmosphere (CRISTA) experiment and middle atmosphere variability, *J. Geophys. Res.*, *104*, 16,311–16,325.
Preusse, P., et al. (2002), Space based measurements of stratospheric mountain waves by CRISTA: 1. Sensitivity, analysis method and a case study, *J. Geophys. Res.*, *107*, 8178, doi:10.1029/2001JD000699.
Preusse, P., et al. (2006), Tropopause to mesopause gravity waves in August: Measurement and modeling, *J. Atmos. Sol. Terr. Phys.*, *68*, 1730–1751.
Randel, W. J., and F. Wu (2005), Kelvin wave variability near the equatorial tropopause observed in GPS radio occultation measurements, *J. Geophys. Res.*, *110*, D03102, doi:10.1029/2004JD005006.
Russell, J. M., III, et al. (1999), An overview of the SABER experiment and preliminary calibration results, *Proc. SPIE*, *3756*, 277–288.
Schmidt, T., et al. (2008), Global gravity wave activity in the tropopause region from CHAMP radio occultation data, *Geophys. Res. Lett.*, *35*, L16807, doi:10.1029/2008GL034986.
Schmidt, T., et al. (2010), Observational characteristics of the tropopause inversion layer derived from CHAMP/GRACE radio occultations and MOZAIC aircraft data, *J. Geophys. Res.*, *115*, D24304, doi:10.1029/2010JD014284.
Smith, E., and S. Weintraub (1953), The constants in the equation for atmospheric refractive index at radio frequencies, *Proc. I.R.E.*, *41*, 1035–1037, doi:10.1109/JRPROC.1953.27429.
Schroeder, S., et al. (2009), Gravity waves resolved in ECMWF and measured by SABER, *Geophys. Res. Lett.*, *36*, L10805, doi:10.1029/2008GL037054.
Tsuda, T., et al. (2004), Characteristics of gravity waves with short vertical wavelengths observed with radiosonde and GPS occultation during DAWEX (Darwin Area Wave Experiment), *J. Geophys. Res.*, *109*, D20S03, doi:10.1029/2004JD004946.
Tsuda, T., et al. (2000), A global morphology of gravity wave activity in the stratosphere revealed by the GPS occultation data (GPS/MET), *J. Geophys. Res.*, *105*, 7257–7273.
Wang, L., and M. J. Alexander (2010), Global estimates of gravity wave parameters from GPS radio occultation temperature data, *J. Geophys. Res.*, *115*, D21122, doi:10.1029/2010JD013860.

Wu, D. L., et al. (2006), Remote sounding of atmospheric gravity waves with satellite limb and nadir techniques, *Adv. Space Res.*, *37*, 2269–2277, doi:10.1016/j.asr.2005.07.031.

Yan, X., et al. (2010), Global observations of gravity waves from High Resolution Dynamics Limb Sounder temperature measurements: A yearlong record of temperature amplitude and vertical wavelength, *J. Geophys. Res.*, *115*, D10113, doi:10.1029/2008JD011511.

Zhang, X., et al. (2012), A global morphology of gravity wave activity in the stratosphere revealed by the 8-year SABER/TIMED data, *J. Geophys. Res.*, *117*, D21101, doi:10.1029/2012JD017676.